Modeling and Analysis of MIMO Multipath Channels with Aerial Intelligent Reflecting Surface

Ma, Zhangfeng; Ai, Bo; He, Ruisi ; Mi, Hang; Yang, Mi ; Wang, Ning ; Zhong, Zhangdui; Fan, Wei

Published in:
I E E E Journal on Selected Areas in Communications

DOI (link to publication from Publisher):
10.1109/JSAC.2022.3196112

Publication date:
2022

Document Version
Accepted author manuscript, peer reviewed version

Modeling and Analysis of MIMO Multipath Channels with Aerial Intelligent Reflecting Surface

Zhangfeng Ma, *Student Member, IEEE*, Bo Ai, *Fellow, IEEE*, Ruisi He, *Senior Member, IEEE*, Hang Mi, *Student Member, IEEE*, Mi Yang, *Student Member, IEEE*, Ning Wang, *Member, IEEE*, Zhangdui Zhong, *Fellow, IEEE*, and Wei Fan, *Senior Member, IEEE*

***Abstract*—Recently, intelligent reflecting surface (IRS) has become a research focus for its capability of controlling the radio propagation environments. Compared to the conventional terrestrial IRS, aerial IRS (AIRS) exploiting unmanned aerial vehicle (UAV)/high-altitude platform (HAP) can provide better deployment flexibility. To this end, a three-dimensional (3D) one-cylinder model is first developed for AIRS-assisted multiple-input multiple-output (MIMO) narrowband channels. In order to change the wireless channel with AIRS and create a favorable propagation environment, we propose a novel method of designing the phase-shifts for the IRS elements. Based on the model, channel impulse response (CIR), space-time correlation function, and channel capacity are derived and thoroughly investigated. A key observation in this paper is that multipath and Doppler effects in radio propagation environments can be effectively mitigated via adjusting the phase-shifts of IRS. More specifically, for the special propagation environments in the absence of any scatterers, it is found that the effects of multipath fading can be completely eliminated by IRSs. While for the general propagation environments with multiple scatterers, a small number of IRS elements can also significantly reduce the Doppler spread and the deep fades in the magnitude of CIR. Based on the numerical investigation of channel correlations, it is shown that channel non-stationarity is not introduced into the time domain when the phase shift of IRS is linear related to the time. Moreover, the channel capacity can also be improved by the proposed methods. Finally, the model with non-ideal IRSs is considered and it is found that using non-ideal IRSs results in poor performances compared with using ideal IRSs. These conclusions will provide a fundamental support for developing intelligent and controllable propagation environments of the future sixth-generation (6G) wireless networks.**

***Index Terms*—Unmanned aerial vehicle (UAV), intelligent reflecting surface (IRS), channel modeling, multiple-input multiple-output (MIMO), propagation characteristics.**

This work was supported by the National Key R&D Program of China under Grant 2021YFB2900301, and 2020YFB1806903, the National Natural Science Foundation of China under Grant 61922012, 62001519, 61725101, U1834210, and 61961130391, the State Key Laboratory of Rail Traffic Control and Safety under Grant RCS2020ZT008, RCS2019ZZ007, and RCS2020ZT010, the Fundamental research funds for the central universities under Grant 2020JBZD005 and I20JB0200030, and China Scholarship Council under Grant 202007090030. This paper was presented in part at the IEEE Globecom 2021. (*Corresponding authors: Bo Ai and Ruisi He.*)

Z. Ma, R. He, H. Mi, M. Yang, and Z. Zhong are with the State Key Laboratory of Rail Traffic Control and Safety, Beijing Engineering Research Center of High-speed Railway Broadband Mobile Communications, and the School of Electronic and Information Engineering, Beijing Jiaotong University, Beijing 100044, China (e-mails: zhangfeng_ma@bjtu.edu.cn; ruisi.he@bjtu.edu.cn; hangmi@bjtu.edu.cn; yangmi_chn@bjtu.edu.cn; zhdzhong@bjtu.edu.cn).

B. Ai is with the State Key Lab of Rail Traffic Control and Safety, Beijing Jiaotong University, and also with Peng Cheng Laboratory and Henan Joint International Research Laboratory of Intelligent Networking and Data Analysis, Zhengzhou University, Zhengzhou 450001, China (e-mail: boai@bjtu.edu.cn).

N. Wang is with the School of Information Engineering, Zhengzhou University, Zhengzhou 450001, China (e-mail: ienwang@zzu.edu.cn).

W. Fan is with the Department of Electronic Systems, Faculty of Engineering and Science, Aalborg University, Aalborg 9220, Denmark (e-mail: wfa@es.aau.dk).

I. Introduction

SINCE intelligent reflecting surface (IRS) is capable of enhancing communication quality in a cost- and energy-efficient way [1]–[3], it is regarded as one of the most promising techniques in the sixth-generation (6G) wireless communications. Current applications of IRS-assisted communications include resource allocation, non-orthogonal multiple access, wireless power transfer, physical layer security [4]–[6], etc. Specifically, IRS is a man-made surface composed of a vast number of passive reflecting elements that can be electronically controlled to reconfigure its electromagnetic (EM) functionalities (e.g., reflection, absorption, polarization, etc.), thereby achieving the purpose of dynamic control of the propagation channel [7]. To better design IRS-assisted communication systems, a detailed knowledge of the underlying wireless channel and the corresponding channel model are urgent needed [8]–[12].

A. Related Work

While IRS has a long history in EM literatures, the corresponding channel measurements and modeling are still in its infancy. Up to now, free-space path loss models for IRS-assisted communications have been studied extensively [13]–[18]. In [13], a simple method was proposed for deriving the expression of path loss. In [14], a low-complexity pathloss model was proposed for terahertz (THz) propagation environments. In [15], a physics-consistent model was proposed for calculating the path loss, which is general enough for application to various operating regimes including near-field and far-field asymptotic regimes. In [16], free-space path loss models were developed for different scenarios by studying the physics and EM nature of IRSs. More recently, based on the path loss models in [16], corresponding models operating in millimeter-wave (mmWave) bands have been proposed in [17]. In [18], a far-field path loss model was derived based on the physical optics techniques. It is worth noting that deterministic channel modeling (e.g. path loss method) needs to carry out large numbers of measurements, which mainly

suitable for specific scenarios. Compared with deterministic models, geometry-based stochastic model (GBSM) has been widely used for describing a variety of IRS-assisted communication scenarios due to its high accuracy and generality [19]–[23]. In [19], a twin cluster channel model was developed for massive multiple-input multiple-output (MIMO) communication scenarios. In [20], a general wideband non-stationary channel model was adopted to depict the MIMO communication environments. In [21], a 3D non-stationary MIMO channel model was proposed for unmanned aerial vehicle (UAV) communications. Furthermore, based on [21], a high-altitude platform (HAP)-MIMO channel model was proposed in [22]. In [23], a 3D cluster-based model was proposed for UAV-MIMO channels. Remarkably, despite the aforementioned works [13]–[23] investigate the impacts of IRS on the statistical properties of wireless channel, the nature of IRS, i.e., creating a smart radio environment between the transmitter (Tx) and the receiver (Rx), is completely ignored. Thus, this also limits the deepening understanding of IRS.

Currently, few works [24], [25] has studied the nature of IRS from the perspective of radio propagation. In [24], a 2D narrowband channel model was first presented for IRS-assisted single-input single-output (SISO) communications. Then, the influences of Doppler effect on the received signal can be effectively reduced by the adjustable phase shifts of the IRS. In [25], a 3D wideband line-of-sight (LoS) channel model was developed for IRS-assisted SISO communications. Then, a multi-objective optimization scheme was proposed for designing the phase-shifts of IRS, which maximizes the instantaneous signal-to-noise ratio (SNR) and minimizes Doppler spread with maintain the delay spread to a relatively low range. However, the channels in [24], [25] are mainly confined to simplistic mathematical models, which will lead to relatively low accuracy and poor generality when employed in the real IRS-assisted communication scenarios, thus affecting the accuracy of IRS technology in the radio propagation environments. Furthermore, the existing works [13]–[25] assumed that each IRS is deployed at fixed locations such as hotspot or cell edge (i.e., terrestrial IRS), which improves the communication performance of its nearby users only. To address this limitation, an effective method is by mounting IRS onto the HAP [26] or UAV [27]–[32] to assist the terrestrial communications, which is named as aerial IRS (AIRS)-assisted communications [33]–[35]. Different from the terrestrial IRS, AIRS can constantly adjust the location of IRS owing to its flexibility and adaptive altitude, so as to maintain the LoS dominated transmission with both Tx and Rx. Consequently, the channel models in aforementioned studies cannot be directly used to characterize the AIRS-assisted communication scenarios. Based on the above analysis, these motivate us to propose a general stochastic channel model that can be used to describe a variety of AIRS-assisted communication scenarios, which aim at efficiently and precisely building smart radio environments.

B. Major Contributions and Novelties

To fill up the above gap, compared with our previous work in [36], the extension for narrowband GBSM for AIRS-assisted communications is proposed. This paper not only proposes more approaches to design the phase shifts of IRS, but also studies more practical phase shift model. The major contributions and novelties of this paper are summarized as follows:

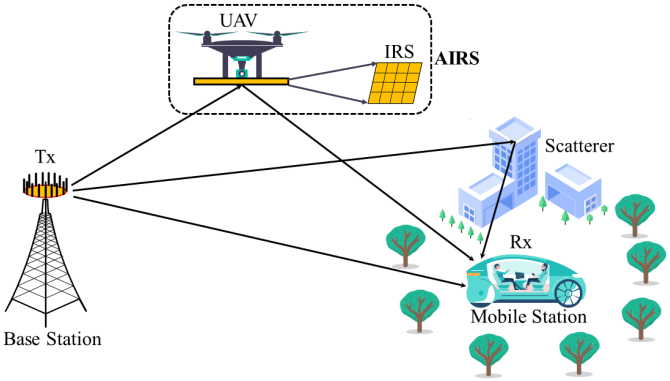

Fig. 1. System model of AIRS-assisted communication system.

- First, we consider an AIRS-assisted network in which an AIRS carries a large array of IRS elements to provide configurable reflecting paths between the Tx and the Rx. Based on the proposed system framework, a geometric MIMO model is proposed for narrowband AIRS-assisted channels. Moreover, the proposed channel model has the ability to adapt for various AIRS-assisted communication scenarios by adjusting the model parameters.
- Next, we propose some novel approaches that adjust the phase shifts of all reflecting elements in real time, which can not only mitigate the Doppler and multipath effects, but also take the tradeoff between Doppler effect mitigation and magnitude of channel impulse response (CIR) maximization into consideration.
- In order to analyze thoroughly the proposed channel model, the expressions of CIR, spreading function, and space-time correlation function, channel capacity are derived and investigated, where the effects of different phase shifts of IRS are considered. A key insight obtained from our analysis is that the multipath and Doppler effects in propagation environments can be effectively mitigated by real-time tunable phase shifts of IRS.
- Finally, some practical issues of the phase design of IRS (e.g., erroneous estimation of Doppler shifts, practical reflection phases, and discrete-time reflection phases) are discussed, which results in performance degradation compared with using ideal IRSs.

The remainder of this paper is organized as follows. Section II describes the geometrical one-cylinder model for AIRS-assisted MIMO channels. The details of the proposed design methods of IRS phase shifts are discussed in Section III. The key statistical properties and capacity of the proposed channel model are derived and analyzed in Section IV. In Section V, numerical simulations and discussions are presented. Some practical issues associated with IRS phase shifts are discussed in Section VI. Finally, Section VII concludes the paper.

II. Three-Dimensional Channel Model

In this paper, we consider a propagation environment consisting of a base station (BS), a mobile station (MS), and an AIRS. By introducing some artificial controlled paths combat multipath fading through the AIRS, the communication performance between the BS and the MS can be improved. Without loss of generality, it is assumed that the Tx and Rx represent the locations of the BS and the MS, respectively. As shown in Fig. 1, the scatterers result in three different propagation modes: LoS mode where waves directly travel from Tx to Rx, single-bounced at the Rx side (SBR) mode where waves scatter from the scatterers located around Rx before arriving at Rx, and single-bounced at the AIRS side (SBA) mode where waves scatter from the AIRS before arriving at Rx.

A. One-Cylinder Scattering Model

Here, a one-cylinder channel model is proposed for AIRS-assisted MIMO communications. For clarity, Fig. 2 shows the LoS and non-LoS (NLoS) paths of the 3D model for a MIMO channel, whereas Fig. 3 shows the projection of this model to the xy plane. The Tx is equipped with L_T transmit omnidirectional antennas, where the adjacent antenna elements are separated by d_T. Similarly, the Rx is equipped with L_R receive omnidirectional antennas, where the adjacent antenna elements are separated by d_R. The AIRS comprises of a uniform linear array (ULA) with N [1] passive reflecting elements, separated by the distance d_A. The orientations of the transmit antenna array in the azimuth plane (relative to the x-axis) and elevation plane (relative to the xy plane) are denoted as φ_T and ψ_T, respectively. Similarly, at the Rx, they are denoted as φ_R and ψ_R, respectively. Because the UAV moves in 3D space, the moving direction of AIRS should be described by the azimuth movement angle γ_A and the elevation movement angle ξ_A, whereas, the Rx only has an azimuth movement angle γ_R. Finally, υ_A and υ_R are the moving velocities of the AIRS and Rx, respectively. The distance between the Tx and Rx is D, H_T, H_A, and H_R represent the heights of Tx, AIRS, and Rx, respectively. The elevation angle between Tx and Rx β_0 is defined as:

$$\beta_0 = \arctan\left(\frac{H_T - H_R}{D}\right), \tag{1}$$

Since in most cases, $H_T \gg H_R$, we can also get β_0 by:

$$\beta_0 \approx \arctan\left(\frac{H_T}{D}\right). \tag{2}$$

The scattering environment at the Rx side is described by a single cylinder geometrical model. Specifically, M omnidirectional scatterers (e.g., buildings and vegetation) are assumed to be on the surface of a cylinder, and the radius of the cylinder is R_R. Parameter $S^{(m)}$ denotes the mth $(m = 1, \ldots, M)$ receive scatterer. Parameter $\alpha_T^{(m)}$ is the azimuth angle of departure (AAoD) of the waves that impinge on the scatterer $S^{(m)}$, whereas $\alpha_R^{(m)}$ is the azimuth angle of arrival (AAoA) of the waves scattered from the scatterer $S^{(m)}$. Similarly, parameter

[1]For simplicity, we assume that a square IRS with $\sqrt{N}$ elements at both horizontal and vertical axes while a generalization is straightforward.

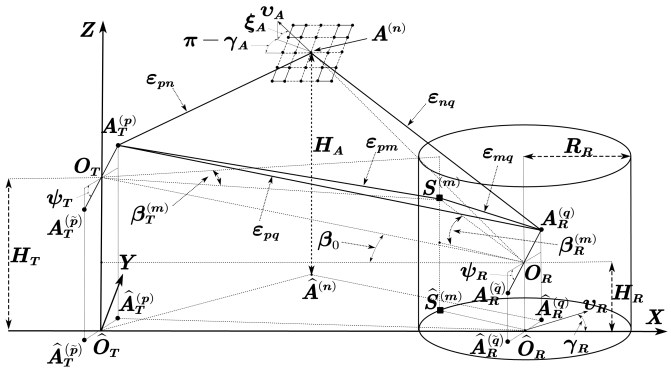

Fig. 2. LoS and NLoS paths of the one-cylinder scattering model for AIRS-assisted MIMO channels.

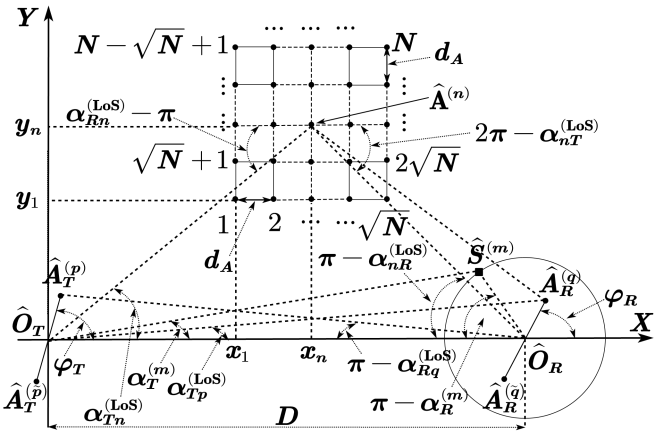

Fig. 3. Projection of the one-cylinder scattering model on the xy plane for AIRS-assisted MIMO channels.

$\beta_T^{(m)}$ denotes the elevation angle of departure (EAoD) of the waves that impinge on the scatterer $S^{(m)}$, whereas $\beta_R^{(m)}$ is the elevation angle of arrival (EAoA) of the waves scattered from the scatterer $S^{(m)}$.

B. Derivation of the Channel Model

The CIR from the pth transmit antenna $A_T^{(p)}$ to the qth receive antenna $A_R^{(q)}$ is calculated as a superposition of the LoS, SBR, and SBA rays [37]–[39], i.e,

$$h_{pq}(t) = h_{pq}^{\mathrm{LoS}}(t) + h_{pq}^{\mathrm{SBR}}(t) + h_{pq}^{\mathrm{SBA}}(t), \tag{3}$$

where $h_{pq}^{\mathrm{LoS}}(t)$, $h_{pq}^{\mathrm{SBR}}(t)$, and $h_{pq}^{\mathrm{SBA}}(t)$ are expressed as

$$h_{pq}^{\mathrm{LoS}}(t) = \sqrt{\frac{K_{\mathrm{Rice}}}{K_{\mathrm{Rice}}+1}} e^{-jk_0\varepsilon_{pq}} e^{j2\pi t f_{D,\mathrm{LoS}}}, \tag{4}$$

$$\begin{aligned} h_{pq}^{\mathrm{SBR}}(t) &= \sqrt{\frac{\eta_{\mathrm{SBR}}}{K_{\mathrm{Rice}}+1}} \frac{1}{\sqrt{M}} \\ &\times \sum_{m=1}^{M} e^{j\phi_m - jk_0(\varepsilon_{pm}+\varepsilon_{mq})} e^{j2\pi t f_{D,m}}, \end{aligned} \tag{5}$$

$$\begin{aligned} h_{pq}^{\mathrm{SBA}}(t) &= \sqrt{\frac{\eta_{\mathrm{SBA}}}{K_{\mathrm{Rice}}+1}} \frac{1}{\sqrt{N}} \\ &\times \sum_{n=1}^{N} e^{-jk_0(\varepsilon_{pn}+\varepsilon_{nq})} e^{j2\pi t f_{D,n}} e^{-j\theta_n(t)}, \end{aligned} \tag{6}$$

where k_0 is the free-space wave number, which is related to the wavelength λ and satisfies $k_0 = 2\pi/\lambda$. Moreover,

TABLE I
DEFINITION OF PARAMETERS IN FIGS. 2 AND 3

Symbol	Definition
R_R	Radii of the cylinder around the Rx.
ε_{ab}	Abbreviation of distance between a and b.
d_A	Spacing between two adjacent reflecting elements at the AIRS.
D, β_0	Distance and elevation angle between the centers of the Tx and Rx, respectively.
H_T, H_R, H_A	Height of Tx, Rx, AIRS, respectively.
d_T, d_R	Spacing between two adjacent antenna elements at the Tx and Rx, respectively.
φ_T, φ_R	Orientation angles of the Tx and Rx antenna array in the xy-plane (relative to the x-axis), respectively.
ψ_T, ψ_R	Elevation angles of the Tx's and Rx's antenna array relative to the xy-plane, respectively.
υ_R, γ_R	Velocity and azimuth direction of Rx, respectively.
υ_A, γ_A (ξ_A)	Velocity and azimuth (elevation) direction of AIRS, respectively.
$\alpha_T^{(m)}$, $\beta_T^{(m)}$	Azimuth angle of departure (AAoD) and elevation angle of departure (EAoD) of the waves that impinge on the scatterer $S^{(m)}$, respectively.
$\alpha_R^{(m)}$, $\beta_R^{(m)}$	Azimuth angle of arrival (AAoA) and elevation angle of arrival (EAoA) of the waves scattered from the scatterer $S^{(m)}$, respectively.
$\alpha_{Tp}^{(\mathrm{LoS})}$, $\alpha_{Rq}^{(\mathrm{LoS})}$	AAoD and AAoA of the LoS path, respectively.
$\alpha_{Tn}^{(\mathrm{LoS})}$, $\beta_{Rn}^{(\mathrm{LoS})}$	AAoD and AAoA of the Tx–AIRS link, respectively.
$\alpha_{nT}^{(\mathrm{LoS})}$, $\beta_{nR}^{(\mathrm{LoS})}$	AAoD and AAoA of the AIRS–Rx link, respectively.

$\theta_n(t) \in [0, 2\pi)$ is the phase shift of the nth IRS element. Furthermore, it is assumed that the each element of the IRS has a unit-amplitude reflection coefficient, and the reflection phase can be continuously adjusted with a very high resolution reflection phase. K_{Rice} denotes the Ricean K-factor. η_{SBR} and η_{SBA} are the weight factors of SBR and SBA, and they satisfy $\eta_{\mathrm{SBR}} + \eta_{\mathrm{SBA}} = 1$. In addition, ε_{pq}, ε_{pm}, ε_{mq}, ε_{pn}, ε_{nq} denote the distances of $A_T^{(p)}$–$A_R^{(q)}$, $A_T^{(p)}$–$S^{(m)}$, $S^{(m)}$–$A_R^{(q)}$, $A_T^{(p)}$–$A^{(n)}$, $A^{(n)}$–$A_R^{(q)}$, respectively. Finally, phase ϕ_m is a random variable with uniform distribution over $[-\pi, \pi)$.

Using the approximation $\sqrt{1+x} \approx 1 + x/2$ for small x and the application of the law of cosines, the propagation distance terms in (4)–(6) can be approximated as

$$\varepsilon_{pq} \approx (D - \Delta_T \cos\psi_T \cos\varphi_T + \Delta_R \cos\psi_R \cos\varphi_R)/\cos\beta_0, \tag{7}$$

$$\begin{aligned}\varepsilon_{pm} \approx{}& D/\cos\beta_0 - \sin\beta_0 \left(R_R \tan\beta_R^{(m)} - \Delta_T \sin\psi_T\right) \\ &- \Delta_T \cos\beta_0 \cos\psi_T \cos\left(\alpha_T^{(m)} - \varphi_T\right),\end{aligned} \tag{8}$$

$$\begin{aligned}\varepsilon_{mq} \approx{}& R_R \Big/ \cos\beta_R^{(m)} - \Delta_R \sin\psi_R \sin\beta_R^{(m)} \\ &- \Delta_R \cos\psi_R \cos\beta_R^{(m)} \cos\left(\alpha_R^{(m)} - \varphi_R\right),\end{aligned} \tag{9}$$

$$\begin{aligned}\varepsilon_{pn} \approx{}& \varepsilon_{\hat{O}_T\hat{A}^{(n)}} \Big/ \cos\beta_{Tn}^{(\mathrm{LoS})} - \Delta_T \sin\psi_T \sin\beta_{Tn}^{(\mathrm{LoS})} \\ &- \Delta_T \cos\psi_T \cos\beta_{Tn}^{(\mathrm{LoS})} \cos\left(\alpha_{Tn}^{(\mathrm{LoS})} - \varphi_T\right),\end{aligned} \tag{10}$$

$$\begin{aligned}\varepsilon_{nq} \approx{}& \varepsilon_{\hat{O}_R\hat{A}^{(n)}} \Big/ \cos\beta_{nR}^{(\mathrm{LoS})} - \Delta_R \sin\psi_R \sin\beta_{nR}^{(\mathrm{LoS})} \\ &- \Delta_R \cos\psi_R \cos\beta_{nR}^{(\mathrm{LoS})} \cos\left(\alpha_{nR}^{(\mathrm{LoS})} - \varphi_R\right),\end{aligned} \tag{11}$$

where the parameter Δ_T is the distance between the pth transmit antenna element and the center of the transmit antenna array. Similarly, parameter Δ_R is the distance between the qth receive antenna element and the center of the receive antenna array. For the ULAs, which can be expressed as

$$\Delta_T = \frac{L_T - 2p + 1}{2} d_T, \tag{12}$$

$$\Delta_R = \frac{L_R - 2q + 1}{2} d_R. \tag{13}$$

The symbols $\varepsilon_{\hat{O}_T\hat{A}^{(n)}}$ and $\varepsilon_{\hat{O}_R\hat{A}^{(n)}}$ denote the distances of $\hat{O}_T$–$\hat{A}^{(n)}$ and $\hat{O}_R$–$\hat{A}^{(n)}$ links, respectively. According to the geometrical relationship, we have

$$\varepsilon_{\hat{O}_T\hat{A}^{(n)}} = \sqrt{(x_n)^2 + (y_n)^2}, \tag{14}$$

$$\varepsilon_{\hat{O}_R\hat{A}^{(n)}} = \sqrt{(D - x_n)^2 + (y_n)^2}, \tag{15}$$

where $x_n = x_1 + \left(n - 1 - a_n\sqrt{N}\right) d_A$, $y_n = y_1 + a_n d_A$, $a_n = \left\lfloor \frac{n-1}{\sqrt{N}} \right\rfloor$, $\lfloor \cdot \rfloor$ denotes the floor function. The symbols x_1 and y_1 are the coordinates of the 1st AIRS element in the xy plane. Based on the assumption that $L_T d_T \ll \varepsilon_{\hat{O}_T\hat{A}^{(n)}}$ and $H_R \ll H_A$, AAoD, AAoA, EAoD, and EAoA of the LoS path for Tx–AIRS link are given by

$$\alpha_{Tn}^{(\mathrm{LoS})} \approx \arcsin\left(y_n \Big/ \varepsilon_{\hat{O}_T\hat{A}^{(n)}}\right), \tag{16}$$

$$\alpha_{Rn}^{(\mathrm{LoS})} \approx \pi + \alpha_{Tn}^{(\mathrm{LoS})}, \tag{17}$$

$$\beta_{Tn}^{(\mathrm{LoS})} = \beta_{Rn}^{(\mathrm{LoS})} \approx \arctan\left((H_A - H_T) \Big/ \varepsilon_{\hat{O}_T\hat{A}^{(n)}}\right). \tag{18}$$

Similarly, AAoD, AAoA, EAoD, and EAoA of the LoS path for AIRS–Rx link can be derived as

$$\alpha_{nT}^{(\mathrm{LoS})} \approx \pi + \alpha_{nR}^{(\mathrm{LoS})}, \tag{19}$$

$$\alpha_{nR}^{(\mathrm{LoS})} \approx \arcsin\left(y_n \Big/ \varepsilon_{\hat{O}_R\hat{A}^{(n)}}\right), \tag{20}$$

$$\beta_{nT}^{(\mathrm{LoS})} = \beta_{nR}^{(\mathrm{LoS})} \approx \arctan\left(H_A \Big/ \varepsilon_{\hat{O}_R\hat{A}^{(n)}}\right). \tag{21}$$

The Doppler terms in (4)–(6) can be derived as

$$f_{D,\mathrm{LoS}} = \frac{\upsilon_R}{\lambda} \cos\left(\alpha_{Rq}^{(\mathrm{LoS})} - \gamma_R\right) \cos\beta_{Rq}^{(\mathrm{LoS})}, \tag{22}$$

$$f_{D,m} = \frac{\upsilon_R}{\lambda} \cos\left(\alpha_R^{(m)} - \gamma_R\right) \cos\beta_R^{(m)}, \tag{23}$$

$$\begin{aligned}f_{D,n} = {}& \tfrac{\upsilon_A}{\lambda} \cos\left(\alpha_{Rn}^{(\mathrm{LoS})} - \gamma_A\right) \cos\beta_{Rn}^{(\mathrm{LoS})} \cos\xi_A \\ &+ \sin\beta_{Rn}^{(\mathrm{LoS})} \sin\xi_A\Big) + \tfrac{\upsilon_A}{\lambda} \cos\left(\alpha_{nT}^{(\mathrm{LoS})} - \gamma_A\right) \\ &\times \cos\beta_{nT}^{(\mathrm{LoS})} \cos\xi_A + \sin\beta_{nT}^{(\mathrm{LoS})} \sin\xi_A\Big) \\ &+ \tfrac{\upsilon_R}{\lambda} \cos\left(\alpha_{nR}^{(\mathrm{LoS})} - \gamma_R\right) \cos\beta_{nR}^{(\mathrm{LoS})},\end{aligned} \tag{24}$$

where $\alpha_{Rq}^{(\mathrm{LoS})} \approx \pi$, $\beta_{Rq}^{(\mathrm{LoS})} \approx \beta_0$.

Moreover, it can be observed from Figs. 2 and 3 that the AoAs and AoDs of SBR ray have some certain geometric relationships to achieve mutual conversion, which can be expressed as

$$\sin\alpha_T^{(m)} \approx \frac{\frac{R_R}{D} \sin\alpha_R^{(m)}}{1 + \frac{R_R}{D} \cos\alpha_R^{(m)}}, \tag{25}$$

$$\cos\alpha_T^{(m)} \approx 1, \tag{26}$$

$$\sin\beta_T^{(m)} \approx \sin\beta_0 - \frac{R_R}{D}\cos^2\beta_0 \cdot a^{(m)}, \tag{27}$$

$$\cos\beta_T^{(m)} \approx \cos\beta_0 + \frac{R_R}{D}\sin\beta_0\cos\beta_0 \cdot a^{(m)}. \tag{28}$$

The derivations of (25)–(28) can be found in Appendix. In addition, it is worth noting that when the number of scatterers approaches infinity ($M \to \infty$), and the discrete azimuth angle $\alpha_R^{(m)}$ and elevation angle $\beta_R^{(m)}$ can be replaced with continuous random variables α_R and β_R, respectively. For the azimuth distribution, the widely used von Mises distribution is adopted [37]–[39], whose probability density function (PDF) is given by

$$f(\alpha_R) = \frac{e^{k\cos(\alpha_R - \alpha_\mu)}}{2\pi I_0(k)}, \tag{29}$$

where $\alpha_R \in [-\pi, \pi]$, $\alpha_\mu \in [-\pi, \pi]$ is the mean angle at which the scatterers are distributed in the horizontal direction, and k controls the spread of scatterers around the mean angle, $I_0(\cdot)$ is the zeroth-order modified Bessel function of the first kind. For the elevation distribution, which is described by the cosine PDF [37]–[39], i.e.,

$$f(\beta_R) = \frac{\pi}{4\beta_m}\cos\left(\frac{\pi}{2}\frac{\beta_R - \beta_\mu}{\beta_m}\right), \tag{30}$$

where $|\beta_R - \beta_\mu| \le |\beta_m| \le \frac{\pi}{2}$. Two parameters β_m and β_μ denote the maximum elevation angle and the mean angle, respectively.

It is apparent that the CIR of SBR relies on the discrete parameters, i.e., $\alpha_R^{(m)}$, and $\beta_R^{(m)}$. In this paper, the modified method of equal areas (MMEA) [22] is used to obtain the discrete sets. Based on the numerical root-finding techniques, the discrete expressions of AAoAs $\left\{\alpha_R^{(m)}\right\}_{m=1}^{M}$ and EAoAs $\left\{\beta_R^{(m)}\right\}_{m=1}^{M}$ can be obtained, respectively, as follows:

$$\frac{m-1/2}{M} - \int_{\alpha_\mu-\pi}^{\alpha_R^{(m)}} f(\alpha_R)d\alpha_R = 0, \tag{31}$$

$$\frac{m-1/2}{M} - \int_{\beta_\mu-\beta_m}^{\beta_R^{(m)}} f(\beta_R)d\beta_R = 0. \tag{32}$$

III. Methods of IRS Phase Shifts for Multipath Propagation Environments

In order to reveal the potential of IRS in multipath propagation environments, it is necessary to propose some effective methods to design the phase shifts of IRS, which are as follows:

1) Method 1: In this method, we set $\theta_n(t) = 0$ for $n = 1, 2, \cdots, N$, which is used to compare with the following benchmark methods.

2) Method 2: In this method, we consider the random phase-shift design for $\theta_n(t)$, where $\theta_n(t)$ for $n = 1, 2, \cdots, N$ is randomly generated following the independent uniform distribution in $[0, 2\pi)$.

3) Method 3: In this method, we aim at improving the Doppler effects in multipath propagation environments by dynamically adjusting the value of the phase shifts. A direct approach is to align the SBA ray with LoS ray, which is given by

$$\begin{aligned}\theta_n(t) = {} & 2\pi\left(f_{D,n} - f_{D,\mathrm{LoS}}\right)t - k_0\left(\varepsilon_{pn} + \varepsilon_{nq}\right) \\ & + k_0\varepsilon_{pq} \pmod{2\pi},\end{aligned} \tag{33}$$

where $n = 1, 2, \cdots, N$.

4) Method 4: In this method, the tradeoff between the Doppler effect mitigation and magnitude of CIR maximization is sufficiently explored by applying extensive search. According to the available number of IRSs, the investigation of our method can be divided into two cases: one is $N \le M$ and the other is $N > M$. By theoretical analysis, we can obtain the optimal values of $\theta_n(t)$ for each case. We discuss these two situations separately:

- **Case 1–Insufficient IRSs:** In the case that the number of IRSs is insufficient compared to the scatterers in multipath propagation environments, we should minimize the effects of the reflections stemming from M scatterers as much as possible by N IRSs. Thus, at each time instant, we need to find all possible permutations of N to M, i.e., a total of $P(M, N)$ [2] permutations. First, we set the IRS phases as

$$\begin{aligned}\theta_n(t) = {} & 2\pi\left(f_{D,n} - f_{D,m}\right)t - k_0\left(\varepsilon_{pn} + \varepsilon_{nq}\right) \\ & + k_0\left(\varepsilon_{pm} + \varepsilon_{mq}\right) - \phi_m - \pi \pmod{2\pi},\end{aligned} \tag{34}$$

  where $n = 1, 2, \cdots, N$, $m = 1, 2, \cdots, M$. Then, the permutation of scatterers that maximizes the magnitude of CIR is selected. Specifically, let us denote the ith permutation (the set of scatterers) by $\mathcal{P}_i = \left\{\mathcal{P}_i^1, \mathcal{P}_i^2, \cdots, \mathcal{P}_i^N\right\}$ for $i = 1, 2, \cdots, P(M, N)$. At a given time instant $t = t_0$, we construct the set of IRS phases as

$$\begin{aligned}\theta_n(t_0) = {} & 2\pi\left(f_{D,n} - f_{D,\mathcal{P}_i^n}\right)t_0 - k_0\left(\varepsilon_{pn} + \varepsilon_{nq}\right) \\ & + k_0\left(\varepsilon_{p\mathcal{P}_i^n} + \varepsilon_{\mathcal{P}_i^n q}\right) - \phi_{\mathcal{P}_i^n} - \pi \pmod{2\pi},\end{aligned} \tag{35}$$

  where $n = 1, 2, \cdots, N$. Based on the obtained results, the optimal set of IRS reflection phases can be obtained

$$\begin{aligned}\hat{\theta}_n(t_0) = {} & 2\pi\left(f_{D,n} - f_{D,\mathcal{P}_{\hat{i}}^n}\right)t_0 - k_0\left(\varepsilon_{pn} + \varepsilon_{nq}\right) \\ & + k_0\left(\varepsilon_{p\mathcal{P}_{\hat{i}}^n} + \varepsilon_{\mathcal{P}_{\hat{i}}^n q}\right) - \phi_{\mathcal{P}_{\hat{i}}^n} - \pi \pmod{2\pi},\end{aligned} \tag{36}$$

  where $n = 1, 2, \cdots, N$. $\mathcal{P}_{\hat{i}}$ denotes the optimal set of scatterers to be targeted by IRSs, where $\hat{i}$ denotes the optimal value of permutation, which can be expressed as $\hat{i} = \arg\max_i |h_{pq}(t_0)|$. Repeat these steps at each time instant until the end of the observation time.
- **Case 2–Sufficient IRSs:** In the case that the number of IRSs is relatively sufficient compared to the scatterers in multipath propagation environments, we should eliminate the reflections from M scatterers as much as possible by N IRSs, while the remaining $N - M$ IRSs are aligned to the LoS ray. Thus, we should thoroughly eliminate the reflections from M scatterers as much as possible by N IRSs, and align the remaining $N - M$ IRS with the LoS ray. Similarly, the number of permutations at

[2] $P(X, Y) = C(X, Y)Y!$, with $X \ge Y$. $C(\cdot, \cdot)$ is the binomial coefficient.

each time instant is $P(N,M)$. Finally, we select the permutation of IRSs that maximizes the magnitude of CIR. Next, we denote the ith permutation (the set of IRSs) by $\mathcal{R}_i = \left\{\mathcal{R}_i^1, \mathcal{R}_i^2, \cdots, \mathcal{R}_i^M\right\}$ and the set of IRSs that are not included in the ith permutation by $\mathcal{S}_i = \left\{\mathcal{S}_i^1, \mathcal{S}_i^2, \cdots, \mathcal{S}_i^{N-M}\right\}$, i.e., $\mathcal{R}_i \cup \mathcal{S}_i = \{1, 2, \cdots, N\}$ for $i = 1, 2, \cdots, P(N,M)$. For a given time instant $t = t_0$, we construct firstly the set of IRS phases to eliminate scatterer reflections as

$$\begin{aligned}&\theta_{\mathcal{R}_i^n}(t_0) = 2\pi\left(f_{D,\mathcal{R}_i^n} - f_{D,n}\right)t_0 - k_0\left(\varepsilon_{p\mathcal{R}_i^n} + \varepsilon_{\mathcal{R}_i^n q}\right)\\&+k_0\left(\varepsilon_{pn} + \varepsilon_{nq}\right) - \phi_n - \pi \pmod{2\pi},\end{aligned} \tag{37}$$

where $n = 1, 2, \cdots, M$, while aligning the remaining $N - M$ IRSs to the LoS ray as follows:

$$\begin{aligned}&\theta_{\mathcal{S}_i^n}(t_0) = 2\pi\left(f_{D,\mathcal{S}_i^n} - f_{D,\mathrm{LoS}}\right)t_0 - k_0\left(\varepsilon_{p\mathcal{S}_i^n} + \varepsilon_{\mathcal{S}_i^n q}\right)\\&+k_0\varepsilon_{pq} \pmod{2\pi},\end{aligned} \tag{38}$$

where $n = 1, 2, \cdots, N - M$. Based on (37), we obtain the optimal set of IRS reflection phases to be paired with scatterers, i.e.,

$$\begin{aligned}&\hat{\theta}_{\mathcal{R}_i^n}(t_0) = 2\pi\left(f_{D,\mathcal{R}_i^n} - f_{D,n}\right)t_0 - k_0\left(\varepsilon_{p\mathcal{R}_i^n} + \varepsilon_{\mathcal{R}_i^n q}\right)\\&+k_0\left(\varepsilon_{pn} + \varepsilon_{nq}\right) - \phi_n - \pi \pmod{2\pi},\end{aligned} \tag{39}$$

where $n = 1, 2, \cdots, M$. $\mathcal{R}_{\hat{i}}$ denotes the optimal set of IRSs to be paired with scatterers, where $\hat{i}$ denotes the optimal value of permutation, which can be expressed as $\hat{i} = \arg\max_i |h_{pq}(t_0)|$. Based on (38), the optimal set of IRS reflection phases to be aligned to the LoS ray can be expressed as

$$\begin{aligned}&\hat{\theta}_{\mathcal{S}_{\hat{i}}^n}(t_0) = 2\pi\left(f_{D,\mathcal{S}_{\hat{i}}^n} - f_{D,\mathrm{LoS}}\right)t_0 - k_0\left(\varepsilon_{p\mathcal{S}_{\hat{i}}^n} + \varepsilon_{\mathcal{S}_{\hat{i}}^n q}\right)\\&+k_0\varepsilon_{pq} \pmod{2\pi},\end{aligned} \tag{40}$$

where $n = M+1, M+2, \cdots, N$. $\mathcal{S}_{\hat{i}}$ denotes the optimal set of IRSs to be aligned to the LoS ray. Repeat these steps at each time instant until the end of the observation time.

Note that although the optimal IRS phase can be obtained by applying extensive search, its complexity increases factorially with the number of scatterers and IRSs, thus limiting its practical applications. Under arbitrary number of scatterers and IRSs, how to obtain the optimal IRS phase by a low-complexity algorithm is left as a future study, while the presented results can be generalized in a systematic way.

IV. Characterization of the AIRS-Assisted MIMO Multipath Channel Models

In this section, the spreading function, space-time correlation function, and channel capacity are derived for the MIMO multipath channels in AIRS-assisted networks by using the proposed channel model.

A. Spreading Function

The movement of the AIRS and MS will bring shift in the carrier frequency, which is called Doppler shift. The spreading function reflects the spreading of the input signal in the Doppler domains, which can be obtained by the Fourier transform of the CIR [40]

$$S_{pq}(f_D) = \int_{-\infty}^{+\infty} h_{pq}(t) \cdot e^{-j2\pi f_D t} dt, \tag{41}$$

where f_D denotes the Doppler shift.

B. Space-Time Correlation Function

Assuming a wide sense stationary condition and a 3D nonisotropic scattering environment, the space-time correlation function can be derived from (3). Since the time-variant CIR of LoS, SBR, and SBA rays are independent zero-mean complex Gaussian random processes in (3), the space-time correlation function with time delay Δt can be expressed as

$$\begin{aligned}&R_{pq,\tilde{p}\tilde{q}}(d_T, d_R, d_A, t, \Delta t) = R^{\mathrm{LoS}}_{pq,\tilde{p}\tilde{q}}(d_T, d_R, d_A, \Delta t)\\&+R^{\mathrm{SBR}}_{pq,\tilde{p}\tilde{q}}(d_T, d_R, d_A, \Delta t) + R^{\mathrm{SBA}}_{pq,\tilde{p}\tilde{q}}(d_T, d_R, d_A, t, \Delta t),\end{aligned} \tag{42}$$

where $p, \tilde{p} \in \{1, \cdots, L_T\}$ and $q, \tilde{q} \in \{1, \cdots, L_R\}$. The terms in (42) are expressed as in (43)–(45)

$$\begin{aligned}&R^{\mathrm{LoS}}_{pq,\tilde{p}\tilde{q}}(d_T, d_R, d_A, \Delta t) = \mathbf{E}\left(\left(h^{\mathrm{LoS}}_{pq}(t)\right)^* \cdot h^{\mathrm{LoS}}_{\tilde{p}\tilde{q}}(t+\Delta t)\right)\\&= \tfrac{K_{\mathrm{Rice}}}{K_{\mathrm{Rice}}+1} e^{jk_0\varepsilon_{pq} - j2\pi t f_{D,\mathrm{LoS}}} e^{-jk_0\varepsilon_{\tilde{p}\tilde{q}} + j2\pi(t+\Delta t)f_{D,\mathrm{LoS}}}\\&= \tfrac{K_{\mathrm{Rice}}}{K_{\mathrm{Rice}}+1} e^{jk_0(\varepsilon_{pq} - \varepsilon_{\tilde{p}\tilde{q}})} e^{j2\pi\Delta t f_{D,\mathrm{LoS}}},\end{aligned} \tag{43}$$

$$\begin{aligned}&R^{\mathrm{SBR}}_{pq,\tilde{p}\tilde{q}}(d_T, d_R, d_A, \Delta t) = \mathbf{E}\left(\left(h^{\mathrm{SBR}}_{pq}(t)\right)^* \cdot h^{\mathrm{SBR}}_{\tilde{p}\tilde{q}}(t+\Delta t)\right)\\&= \tfrac{\eta_{\mathrm{SBR}}}{K_{\mathrm{Rice}}+1}\tfrac{1}{M}\sum_{m=1}^{M}\mathbf{E}\left\{e^{jk_0(\varepsilon_{pm}+\varepsilon_{mq})} e^{-j2\pi t f_{D,m}}\right.\\&\left.\times e^{-jk_0(\varepsilon_{\tilde{p}m}+\varepsilon_{m\tilde{q}})} e^{j2\pi(t+\Delta t)f_{D,m}}\right\}\\&= \tfrac{\eta_{\mathrm{SBR}}}{K_{\mathrm{Rice}}+1}\tfrac{1}{M}\sum_{m=1}^{M} e^{jk_0(\varepsilon_{pm} - \varepsilon_{\tilde{p}m} + \varepsilon_{mq} - \varepsilon_{m\tilde{q}})} e^{j2\pi\Delta t f_{D,m}},\end{aligned} \tag{44}$$

$$\begin{aligned}&R^{\mathrm{SBA}}_{pq,\tilde{p}\tilde{q}}(d_T, d_R, d_A, t, \Delta t) = \mathbf{E}\left(\left(h^{\mathrm{SBA}}_{pq}(t)\right)^* \cdot h^{\mathrm{SBA}}_{\tilde{p}\tilde{q}}(t+\Delta t)\right)\\&= \tfrac{\eta_{\mathrm{SBA}}}{K_{\mathrm{Rice}}+1}\tfrac{1}{N}\sum_{n=1}^{N}\mathbf{E}\left\{e^{jk_0(\varepsilon_{pn}+\varepsilon_{nq})} e^{j\theta_n(t) - j2\pi t f_{D,n}}\right.\\&\left.\times\, e^{-jk_0(\varepsilon_{\tilde{p}n}+\varepsilon_{n\tilde{q}})} e^{j2\pi(t+\Delta t)f_{D,n}} e^{-j\theta_n(t+\Delta t)}\right\}\\&= \tfrac{\eta_{\mathrm{SBA}}}{K_{\mathrm{Rice}}+1}\tfrac{1}{N}\sum_{n=1}^{N}\mathbf{E}\left\{e^{jk_0(\varepsilon_{pn} - \varepsilon_{\tilde{p}n} + \varepsilon_{nq} - \varepsilon_{n\tilde{q}})} e^{j2\pi\Delta t f_{D,n}}\right.\\&\left.\times e^{j(\theta_n(t) - \theta_n(t+\Delta t))}\right\}\\&= \tfrac{\eta_{\mathrm{SBA}}}{K_{\mathrm{Rice}}+1}\tfrac{1}{N} e^{jk_0(\varepsilon_{pn} - \varepsilon_{\tilde{p}n} + \varepsilon_{nq} - \varepsilon_{n\tilde{q}})} e^{j2\pi\Delta t f_{D,n}}\\&\times \sum_{n=1}^{N}\mathbf{E}\left\{e^{j(\theta_n(t) - \theta_n(t+\Delta t))}\right\},\end{aligned} \tag{45}$$

where $(\cdot)^*$ is the complex conjugate operation and $\mathbf{E}[\cdot]$ is the statistical expectation operator.

C. Channel Capacity

The instantaneous MIMO channel capacity of the proposed model, given perfect channel information at the Rx, can be expressed as [41]

$$C(t) = \log_2\left(\det\left(\mathbf{I}_{L_R} + \frac{\rho}{L_T}\mathbf{H}(t)\,\mathbf{H}^H(t)\right)\right), \tag{46}$$

where $L_T \geq L_R$, $\det(\cdot)$ denotes the matrix determinant, $\mathbf{I}_{L_R}$ is an $L_R \times L_R$ identity matrix, ρ is the average receive SNR,

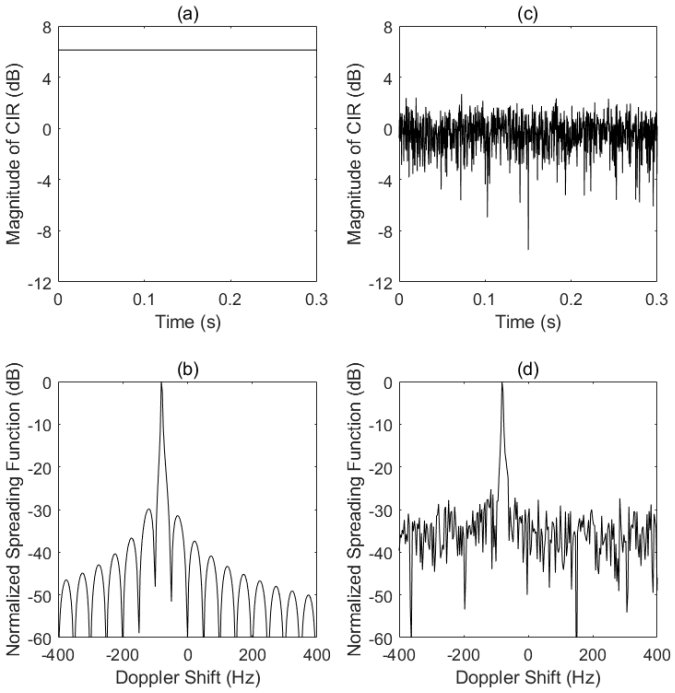

Fig. 4. Generated the magnitude of CIR and normalized spreading function (dB-scaled) using the Method 3. (a)–(b): $M = 0$, $N = 16$. (c)–(d): $M = 16$, $N = 0$.

$(\cdot)^H$ denotes the transpose conjugate operation. Since the time-varying channel matrix $\mathbf{H}_{pq}(t) = [h_{pq}(t)]$ is deterministic of time t, the channel capacity of the simulation model should be analyzed by using time averages, i.e.,

$$m_C = \lim_{T\to\infty} \frac{1}{2T} \int_{-T}^{T} C(t)dt. \tag{47}$$

V. Numerical Results and Analysis

In this section, the impacts of the proposed AIRS reflecting phases on statistical characteristics and capacity of MIMO channel are numerically analyzed based on the above derivations. The parameters for the following numerical analysis are listed here or specified otherwise: $\eta_{\mathrm{SBR}} = 0.2$, $\eta_{\mathrm{SBA}} = 0.8$, $\lambda = 0.125$ m, $K_{\mathrm{Rice}} = 6$ dB, $d_A = 0.1\lambda$, $d_T = d_R = 0.5\lambda$, $p = q = \tilde{p} = \tilde{q} = 2$, $L_T = L_R = 2$, $\varphi_T = \varphi_R = 45$ degrees, $\psi_T = \psi_R = 30$ degrees, $R_R = 10$ m, $H_T = 30$ m, $D = 500$ m, $x_1 = y_1 = 100$ m, $H_A = 120$ m, $k = 2$, $\alpha_\mu = 270$ degrees, β_μ = 0 degree, β_m = 15 degrees, $\upsilon_R = 10$ m/s, $\gamma_R = 0$ degrees, $\upsilon_A = 1$ m/s, γ_A = 180 degrees, ξ_A = 0 degree.

A. CIR and Spreading Function

Fig. 4 illustrates the magnitude of CIR and normalized spreading function for different values of M and N. When $M = 0$, $N = 16$ (i.e., without any scatterers), it is clear from Fig. 4(a) that the magnitude of CIR remains a constant value by applying Method 3, which means that the IRSs have completely controlled the wireless propagation environment. Furthermore, the normalized spreading function of Fig. 4(b) shows that the received signal is still subject to a Doppler shift of -79.86 Hz. The reason is that the LoS ray between Tx and Rx is not controlled by the IRS, and it is impossible to completely eliminate the Doppler shift in this propagation scenario. When $M = 16$, $N = 0$ (i.e., without any IRSs), the obtained magnitude of CIR and normalized spreading function have totally different shape compared to the results in Figs. 4(a)–(b). It is found from Figs. 4(c)–(d) that the magnitude of CIR and normalized spreading function have a very fast fade pattern, which means that the propagation environment is complete random and uncontrollable.

To validate the validity of the proposed algorithm, two status based on the available number of IRSs are considered, i.e., Case 1: $M = 9$, $N = 4$, and Case 2: $M = 4$, $N = 9$. Fig. 5 illustrates the magnitude of CIR and normalized spreading function in Case 1 with different phase selection methods. In Case 1, it is found that:

- For Method 1, due to the destruction and construction of the arriving signals of LoS, SBA, SBR rays, the magnitude of CIR fluctuates rapidly around a mean value. Furthermore, the magnitude of CIR also exhibits a faster fade pattern. For the spreading function, some variations and two sharp components, i.e., -79.86 Hz (from the LoS ray) and 86.28 Hz (from the SBA ray), can be observed in Fig. 5(b). This is because the CIR of LoS and SBA rays are determined; whereas the CIR of SBR ray is random.
- Random phase of IRS results in significantly increased degree of randomness. Compared to the result in Fig. 5(a), stronger randomness and variations can be observed in the magnitude of CIR. Furthermore, only one sharp component from LoS ray can be observed in the spreading function.
- Compared to the results in Method 1, although the Method 3 can eliminate the SBA component in the spreading function, a noticeable fade pattern can still be observed in the magnitude of CIR due to uncontrollable reflections from SBR ray. This implies that the radio propagation environments are somewhat controlled by utilizing real-time tunable IRS. Significantly, however, Method 3 ensures a higher magnitude of CIR, but it comes at the cost of a faster variation in time.
- Although Method 4 also can reduce the fade patterns, an tradeoff between the Doppler effect mitigation and magnitude of CIR maximization in the time domain is not observed significantly. The reason is that the number of IRS is less than the number of scatterers, which is not enough to completely eliminate the impact of SBR ray.

Fig. 6 shows the magnitude of CIR and normalized spreading function in Case 2 with different phase selection methods. Compared with the results in Fig. 5, it is found that the variation ranges in magnitude of CIR are significantly smaller, which implies that when the number of IRSs is more than the number of scatterers, the wireless propagation environments can be more effectively controlled. Furthermore, it is worth noting that Method 4 has achieved a better tradeoff between the Doppler effect mitigation and magnitude of CIR maximization. Finally, a slight increase in the magnitude of CIR can also be observed. The reason is that they utilize IRSs to

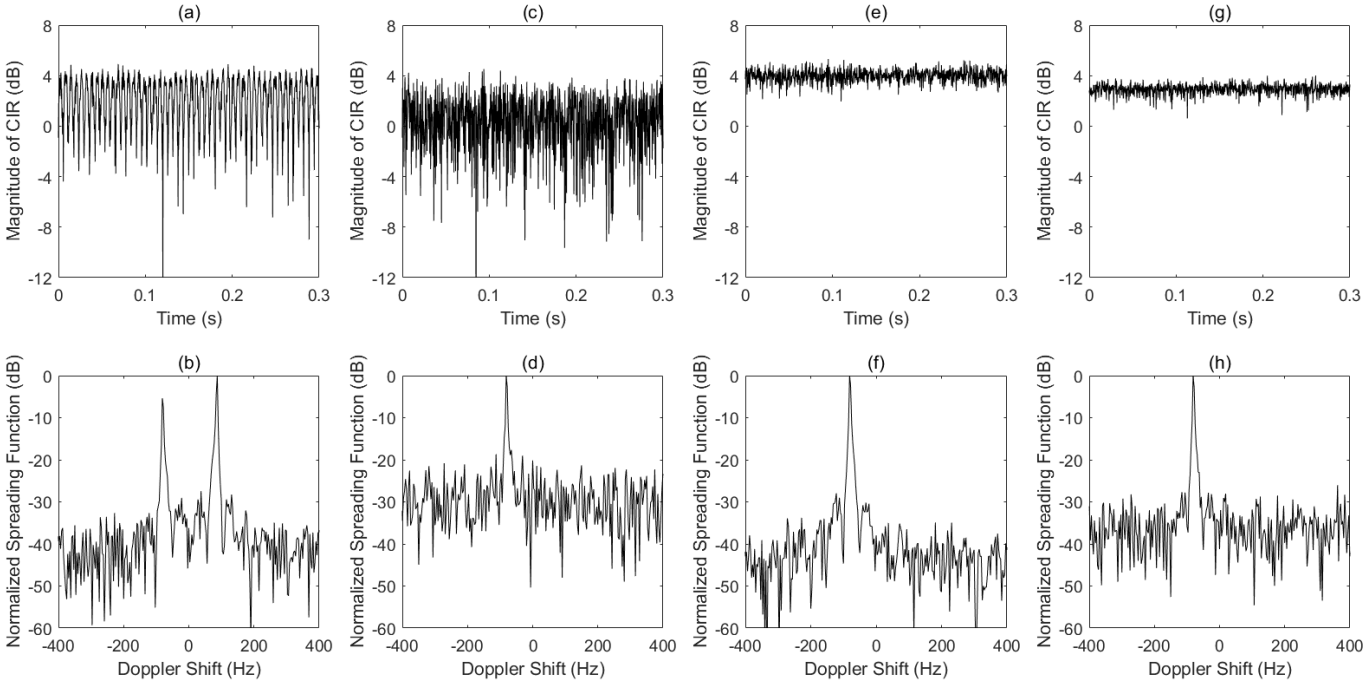

Fig. 5. Generated magnitude of CIR and normalized spreading function (dB-scaled) using the different phase shift design methods, where $M = 9$, $N = 4$. (a)–(b): Method 1. (c)–(d): Method 2. (e)–(f): Method 3. (g)–(h): Method 4.

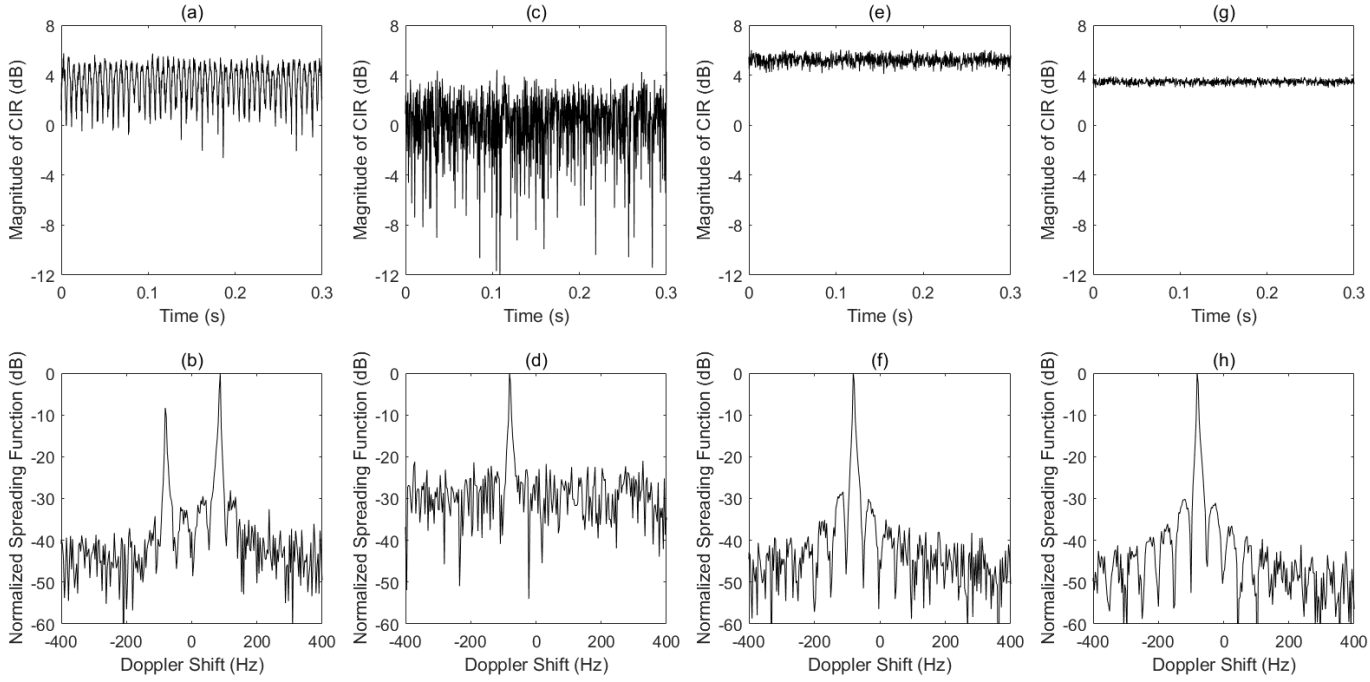

Fig. 6. Generated magnitude of CIR and normalized spreading function (dB-scaled) using the different phase shift design methods, where $M = 4$, $N = 9$. (a)–(b): Method 1. (c)–(d): Method 2. (e)–(f): Method 3. (g)–(h): Method 4.

TABLE II
COMPARISON OF METHODS 1–4 IN TERMS OF PEAK-TO-PEAK VARIATION (Δh_{pq} in dB) AND TIME-AVERAGE ($\bar{h}_{pq}$ in dB) OF $|h_{pq}(t)|$.

	Method 1	**Method 2**	**Method 3**	**Method 4**
$M = 9$, $N = 4$	$\Delta_{h_{pq}} = 14.7$ dB $\bar{h}_{pq} = 1.89$ dB	$\Delta_{h_{pq}} = 19.13$ dB $\bar{h}_{pq} = -0.01$ dB	$\Delta_{h_{pq}} = 3.09$ dB $\bar{h}_{pq} = 4$ dB	$\Delta_{h_{pq}} = 3.11$ dB $\bar{h}_{pq} = 2.93$ dB
$M = 4$, $N = 9$	$\Delta_{h_{pq}} = 7.48$ dB $\bar{h}_{pq} = 3.39$ dB	$\Delta_{h_{pq}} = 19.28$ dB $\bar{h}_{pq} = -0.01$ dB	$\Delta_{h_{pq}} = 2.01$ dB $\bar{h}_{pq} = 5.18$ dB	$\Delta_{h_{pq}} = 0.98$ dB $\bar{h}_{pq} = 3.48$ dB

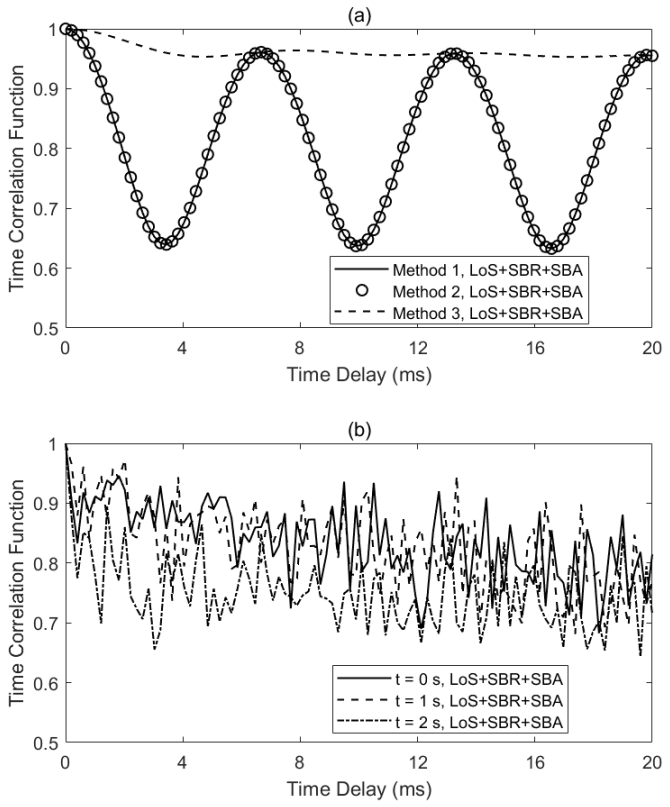

Fig. 7. Absolute value of time correlation functions with different phase shift design methods, where $M = 4$, $N = 9$. (a) Absolute value of time correlation functions for Methods 1–3. (b) Absolute value of time correlation functions for Method 4 at different time instants.

cancel out reflections from scatterers.

To draw more insights, we further provide a quantitative analysis by comparing the peak-to-peak value Δh_{pq} of $|h_{pq}(t)|$ and its time average $\bar{h}_{pq}$ for all methods, as shown in Table II. More specifically, we define $\Delta h_{pq} = |h_{pq}(t)|_{\max} - |h_{pq}(t)|_{\min}$ and $\bar{h}_{pq} = \frac{1}{n_s}\sum_{n=0}^{n_s-1} |h_{pq}(it_s)|$. n_s and t_s respectively stand for the total number of time samples and sampling time, which are selected as $n_s = 960$ and $t_s = 0.3128$ ms for this specific simulation. All the results are averaged over 1000 independent experiments. It can be seen from Table II that the Δh_{pq} of $|h_{pq}(t)|$ obtained by other Methods except Method 2 significantly decreases with the increase of the number of IRSs, while $\bar{h}_{pq}$ significantly increases with the increase of the number of IRSs. In addition, due to the strong LoS ray, Method 3 is a preferred choice for maximizing the time-averaged magnitude of the CIR. Finally, when the number of IRSs is more than the number of scatterers, it is found that Method 4 provides a minimum $\Delta_{h_{pq}}$ and a slightly larger $\bar{h}_{pq}$ compared with Methods 1–3.

B. Time Correlation Function

Fig. 7 illustrates the absolute value of the time correlation function with different phase selection methods. From Fig. 7(a), it is found that the obtained correlation curve using Method 1 has totally the same shape compared to the result using Method 2, and changes rapidly with delay. Furthermore,

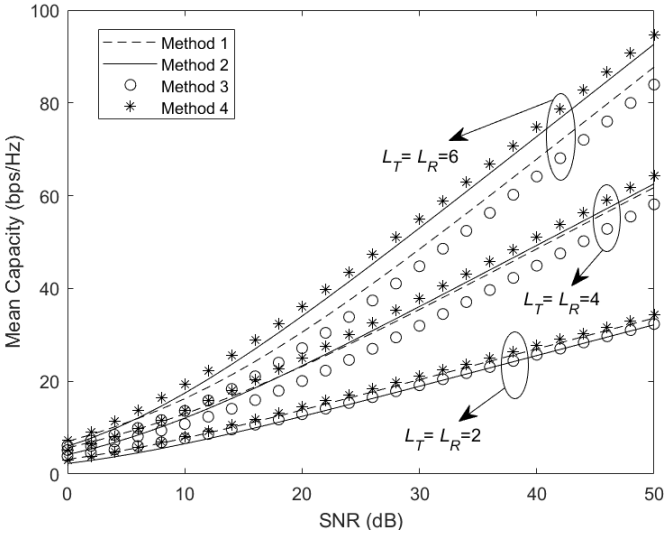

Fig. 8. Mean capacity of a MIMO channel for different phase shift design methods, where $M = 9$, $N = 4$.

the obtained correlation curve using Method 3 changes slowly with delay due to the presence of dominating LoS ray. Remarkably, despite the generated phase shift using the Method 3 is adjusted in real time, the non-stationarity of channel is not introduced in the time domain due to the phase shift of IRSs linearly related to the time. In addition, it is worth noting that since the generated IRS phase shift using the Method 4 has not the explicit expression, the integral in function (45) is solved by weighted average method. All the results are averaged over 1000 independent experiments. Since the relationship between phase shift of IRS and time is nonlinear, the correlation curve obtained using Method 4 varies with time t. To highlight these changes, Fig. 7(b) shows the obtained correlation functions at three time instants, i.e., $t = 0$ s, $t = 1$ s, and $t = 2$ s. It is found that the time correlation functions change with both delay and time rapidly. These findings indicate that although Method 4 also can eliminate the multipath and Doppler effects, which results in non-stationarity in the time domain.

C. Channel Capacity

Fig. 8 illustrates the mean capacity of the various methods against SNR for different numbers of antennas at both the Tx and Rx. When $L_T = L_R = 2$, it is found that the channel capacity obtained from Method 4 is slightly higher than that of Method 1. In addition, we can also see that with the increase in number of antennas, the gap between the two cases is widening.

Fig. 9 shows the cumulative distribution function (CDF) of the mean capacity for the MIMO channel for different phase selection methods when SNR is 10 dB. It is found that the proposed phase shift can be used to deliberately create favorable channel conditions which enhances the mean capacity of MIMO channel.

VI. Practical Issues

The above analysis is based on the ideal IRS communication scenarios. However, the IRSs in practice are usually non-

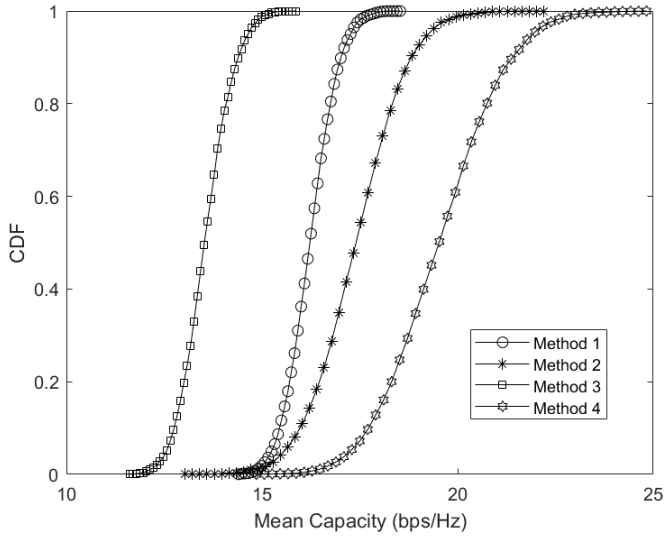

Fig. 9. CDF of the mean capacity of a MIMO channel for different phase shift design methods, where SNR = 10 dB, $L_T = L_R = 2$, $M = 4$, $N = 9$.

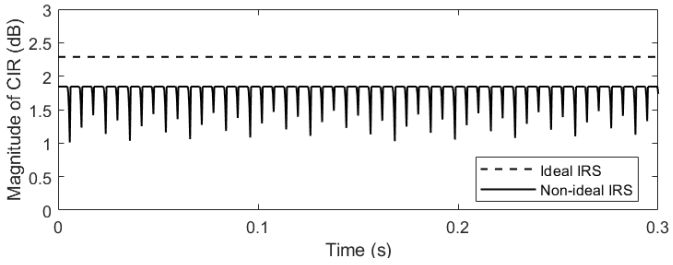

Fig. 10. The comparison of magnitude of CIR obtained using the method 3 between the situations with ideal and non-ideal IRS cases, where $M = 0$, $N = 1$.

ideal due to the limitations of hardware implementation of metamaterials. To evaluate the performance in non-ideal IRS phase shift cases, we consider the several practical issues related IRS applications in this section.

A. Realistic IRSs

Since the amplitude and the phase-shift of reflecting elements are important factors affecting the practical applications, a realistic IRS with a reflection amplitude of –1 dB and a reflection phase between -150° and 140° is considered in [42]. In Fig. 10, we take a comparison of the magnitude of CIR between the situations with ideal and non-ideal IRS. From this figure, it is clear that the non-ideal IRS can cause the degradation of the magnitude of CIR. Meanwhile, this figure also shows that a limited range of phase shift of IRS can cause serious distortion of the waveform.

B. Imperfect Knowledge of Doppler Frequencies

In order to implement the phase design algorithms proposed in Section III, the IRS controller needs to acquire the Doppler frequencies of all incoming rays. However, in the actual IRS-assisted communication scenarios, errors occur in the Doppler shifts received by the IRS controller due to the erroneous estimation of Rx velocity and/or scatterer position. For the sake

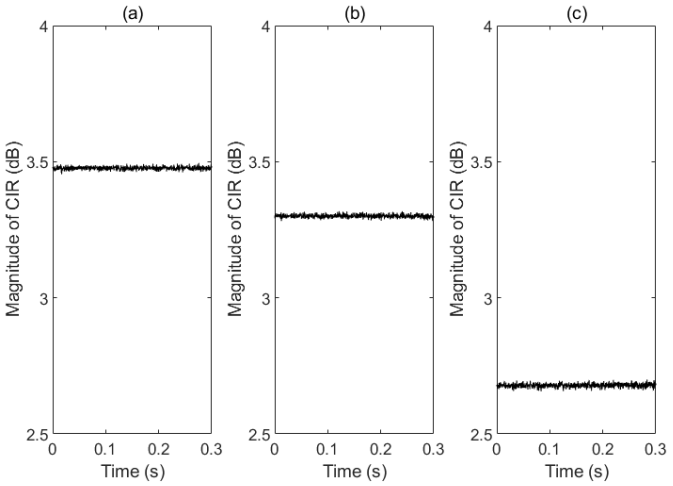

Fig. 11. The comparison of magnitude of CIR obtained using the method 4 for different error of Doppler frequency shifts at IRS, where $M = 4$, $N = 9$. (a) $e_{\max} = 0$. (b) $e_{\max} = 1$. (c) $e_{\max} = 2$.

of brevity, we use Method 3 an example for the discussions and illustrations in this subsection. For the sake of research, it is assumed that the Doppler shift of LoS ray is perfectly known and that of NLoS ray is erroneous. Furthermore, we model the practically estimated Doppler shifts $f^e_{D,n}$ as

$$f^e_{D,n} = f_{D,n} + e_{D,n}, \tag{48}$$

where $e_{D,n}$ is the estimation error with uniform distribution, i.e., $e_{D,n} \sim U[-e_{\max}, e_{\max}]$, where $e_{\max}$ is the maximum estimation error. Fig. 11 presents the magnitude of the CIRs at different estimation errors of Doppler frequency based on 1000 simulation experiments. It is found that the magnitude of the CIR significantly decreases with the increase of $e_{\max}$, which implies that the proposed method for designing the IRS phase shifts is highly sensitive to this type of error.

C. Discrete Phase Shifts of IRS

Due to hardware constraints, the phase shifts of IRS need to be quantized into discrete values, which means that the IRS reflection phases can be tuned at only (certain) discrete-time instants. Therefore, in this subsection, we investigate the impact of discrete phase shifts on the proposed methods, taking Method 3 as an example for discussions and illustrations. Furthermore, it is assumed that once the IRS reflection phases are adjusted according to the LoS ray, they remain fixed for Qt_s seconds.

The generated magnitude of CIR and phase shift of IRS using the Method 3 for different duration of fixed reflection phases are shown in Figs. 12(a)–(b). From Fig. 12(b), it is found that the phase shift of IRS show periodicity over observation time, which shows the IRS controller should update the reflection phases in a real-time manner to meet with the time-varying property of the channel. In addition, it can be also observed that the changing frequency of phase shift of IRS decreases with the increase of Q.

The generated magnitude of CIR and phase shift of IRS using the Method 3 for different velocities of Rx are shown in

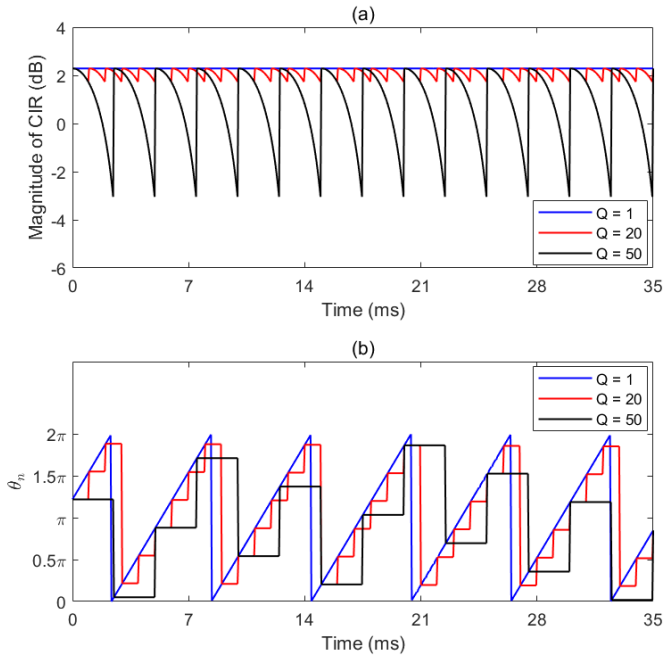

Fig. 12. Generated magnitude of CIR and phase shift of IRS using the Method 3 for different duration of fixed reflection phases, where $M = 0$, $N = 1$, $v_R = 10$ m/s, $t_s = 50$ μs.

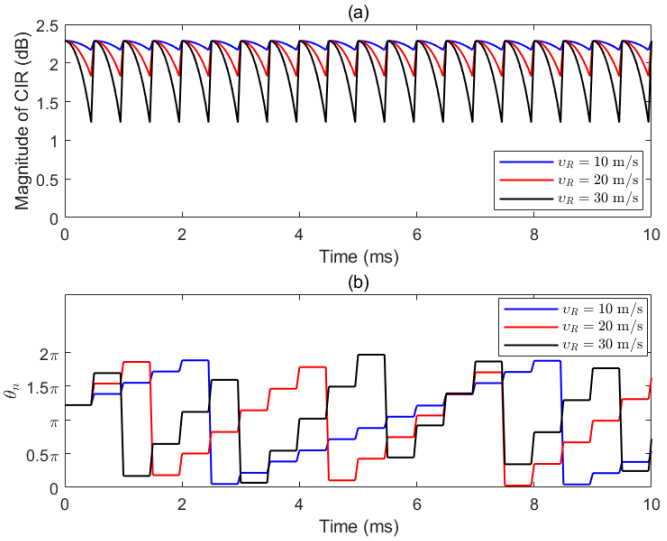

Fig. 13. Generated magnitude of CIR and phase shift of IRS using the Method 3 for different velocities of Rx, where $M = 0$, $N = 1$, $Q = 10$, $t_s = 50$ μs.

Figs. 13(a)–(b). From Fig. 13(a), it is found that magnitude of CIR oscillates more with the increase of the velocity of Rx. Furthermore, it is found from Fig. 13(b) that the changing frequency of phase shift of IRS increases with the increase of the velocity of Rx. Therefore, the increasing velocity of Rx for the proposed IRS-assisted communication systems are challenging, which makes it difficult to adjust IRS reflection phases in real time.

VII. Conclusions

In this paper, a one-cylinder-based 3D MIMO geometrical channel model is proposed for AIRS-assisted MIMO communications, which has the ability to effectively reveal the programmable property of AIRS. The scattering environment is modeled with a few scatterers located on the surface of a cylinder centered on the Rx. To create smart radio environments, we propose several novel methods of optimizing the phase-shifts at the RIS elements. Then, channel statistical properties of proposed channel model, including CIR, spreading function, space-time correlation function, and channel capacity are thoroughly derived and simulated. It is found that the multipath and Doppler effects caused by the movement of Rx can be effectively mitigated by real-time tuneable IRSs. Furthermore, a tradeoff between magnitude of CIR maximization and Doppler effect mitigation is achieved. Based on a detailed investigation of channel correlation function, it is found that when the phase shift of IRS is linear related to the time, non-stationarity is not introduced into the time domain. By contrast, when the relationship between phase shift of IRS and time is nonlinear, which leads to non-stationarity in time domain. In addition, MIMO channel capacity can be also improved by the proposed design methods of IRS phase shift. Finally, the model is implemented with non-ideal IRSs, which leads to performance reduction compared with using ideal IRSs. The proposed methodology provides a theoretical framework for developing intelligent and controllable radio environments.

As a future work, it is important to propose some optimization algorithms with low complexity to design the phase shifts of IRS based on the proposed channel models [43]–[45]. In addition, channel modeling for AIRS-assisted mmWave communication systems is also worth studying [46]–[49].

Appendix

Using the cosine theorem to $\Delta_{\hat{O}_T\hat{S}^{(m)}\hat{O}_R}$ in Fig. 3, we can obtain

$$\left(\varepsilon_{\hat{O}_T\hat{S}^{(m)}}\right)^2 = D^2 + (R_R)^2 + 2R_R D\cos\alpha_R^{(m)}. \tag{49}$$

Since $R_R/D \ll 1$, $(R_R/D)^2$ is very small. $\varepsilon_{\hat{O}_T\hat{S}^{(m)}}$ can be derived as

$$\varepsilon_{\hat{O}_T\hat{S}^{(m)}} = D + R_R\cos\alpha_R^{(m)}. \tag{50}$$

Using the law of sines, we can obtain

$$\sin\alpha_T^{(m)} \approx \frac{\frac{R_R}{D}\sin\alpha_R^{(m)}}{1+\frac{R_R}{D}\cos\alpha_R^{(m)}}, \tag{51}$$

$$\cos\alpha_T^{(m)} \approx 1. \tag{52}$$

From Fig. 2, we can get

$$D\tan\beta_0 = \varepsilon_{\hat{O}_T\hat{S}^{(m)}}\tan\beta_T^{(m)} + R_R\tan\beta_R^{(m)}. \tag{53}$$

Then, $\sin\beta_T^{(m)}$ and $\cos\beta_T^{(m)}$ $\left(\beta_T^{(m)} \in \left(0, \frac{\pi}{2}\right)\right)$ can be expressed as

$$\sin\beta_T^{(m)} = \frac{\tan\beta_0 - \frac{R_R}{D}\tan\beta_R^{(m)}}{\sqrt{\left(1+\frac{R_R}{D}\cos\alpha_R^{(m)}\right)^2 + \left(\tan\beta_0 - \frac{R_R}{D}\tan\beta_R^{(m)}\right)^2}}, \tag{54}$$

$$\cos\beta_T^{(m)} = \frac{1+\frac{R_R}{D}\cos\alpha_R^{(m)}}{\sqrt{\left(1+\frac{R_R}{D}\cos\alpha_R^{(m)}\right)^2+\left(\tan\beta_0-\frac{R_R}{D}\tan\beta_R^{(m)}\right)^2}}. \quad (55)$$

Hence, $\sin\beta_T^{(m)}$ and $\cos\beta_T^{(m)}$ can be further expressed as follows:

$$\sin\beta_T^{(m)} \approx \sin\beta_0 - \frac{R_R}{D}\cos^2\beta_0 \cdot a^{(m)}, \quad (56)$$

$$\cos\beta_T^{(m)} \approx \cos\beta_0 + \frac{R_R}{D}\sin\beta_0\cos\beta_0 \cdot a^{(m)}, \quad (57)$$

where $a^{(m)} = \sin\beta_0\cos\alpha_R^{(m)} + \cos\beta_0\tan\beta_R^{(m)}$.

REFERENCES

[1] W. Saad, M. Bennis and M. Chen, "A vision of 6G wireless systems: Applications, trends, technologies, and open research problems," *IEEE Network*, vol. 34, no. 3, pp. 134–142, May/Jun. 2020.

[2] P. Yang, Y. Xiao, M. Xiao and S. Li, "6G wireless communications: Vision and potential techniques," *IEEE Network*, vol. 33, no. 4, pp. 70–75, Jul./Aug. 2019.

[3] Z. Zhang, Y. Xiao, Z. Ma, M. Xiao, Z. Ding, X. Lei, G. K. Karagiannidis, and P. Fan, "6G wireless networks: Vision, requirements, architecture, and key technologies," *IEEE Vehicular Technology Magazine*, vol. 14, no. 3, pp. 28–41, Sept. 2019.

[4] Q. Wu and R. Zhang, "Towards smart and reconfigurable environment: Intelligent reflecting surface aided wireless network," *IEEE Communications Magazine*, vol. 58, no. 1, pp. 106–112, Jan. 2020.

[5] W. Tang, M. Chen, J. Dai, Y. Zeng, X. Zhao, S. Jin, Q. Cheng, and T. J. Cui, "Wireless communications with programmable metasurface: New paradigms, opportunities, and challenges on transceiver design," *IEEE Wireless Communications*, vol. 27, no. 2, pp. 180–187, Apr. 2020.

[6] M. Di Renzo, A. Zappone, M. Debbah, M. Alouini, C. Yuen, J. de Rosny, and S. Tretyakov, "Smart radio environments empowered by reconfigurable intelligent surfaces: How it works, state of research, and the road ahead," *IEEE Journal on Selected Areas in Communications*, vol. 38, no. 11, pp. 2450–2525, Nov. 2020.

[7] E. Basar and I. Yildirim, "Reconfigurable intelligent surfaces for future wireless networks: A channel modeling perspective," *IEEE Wireless Communications*, vol. 28, no. 3, pp. 108–114, Jun. 2021.

[8] R. He, B. Ai, G. Wang, M. Yang, C. Huang and Z. Zhong, "Wireless channel sparsity: Measurement, analysis, and exploitation in estimation," *IEEE Wireless Communications*, vol. 28, no. 4, pp. 113–119, Aug. 2021.

[9] H. Wang, W. Wang, Y. Wu, B. Tang, W. Zhang and Y. Liu, "Probe selection for 5G massive MIMO base station over-the-air testing," *IEEE Antennas Wireless Propagation Letters*, vol. 19, no. 11, pp. 1998–2002, Nov. 2020.

[10] Y. Lyu, A. W. Mbugua, K. Olesen, P. Kyösti and W. Fan, "Design and validation of the phase-compensated long-range sub-THz VNA-based channel sounder," *IEEE Antennas and Wireless Propagation Letters*, vol. 20, no. 12, pp. 2461–2465, Dec. 2021.

[11] F. Zhang, H. Gao, Z. Wang and W. Fan, "An improved complex signal-based calibration method for beam-steering phased array," *IEEE Antennas and Wireless Propagation Letters*, vol. 20, no. 11, pp. 2161–2165, Nov. 2021.

[12] M. Li, X. Chen, A. Zhang, A. A. Kishk and W. Fan, "Reducing correlation in compact arrays by adjusting near-field phase distribution for MIMO applications," *IEEE Transactions on Vehicular Technology*, vol. 70, no. 8, pp. 7885–7896, Aug. 2021.

[13] S. W. Ellingson, "Path loss in reconfigurable intelligent surface-enabled channels," in *Proc. IEEE PIMRC*, 2021, pp. 1–7.

[14] A. A. Boulogeorgos and A. Alexiou, "Pathloss modeling of reconfigurable intelligent surface assisted THz wireless systems," in *Proc. IEEE ICC*, 2021, pp. 1–6.

[15] F. H. Danufane, M. Di Renzo, J. De Rosny and S. Tretyakov, "On the path-loss of reconfigurable intelligent surfaces: An approach based on Green's theorem applied to vector fields," *IEEE Transactions on Communications*, vol. 69, no. 8, pp. 5573–5592, Aug. 2021.

[16] W. Tang, M. Chen, X. Chen, J. Dai, Y. Han, M. Di Renzo, Y. Zeng, S. Jin, Q. Cheng, T. Cui, "Wireless communications with reconfigurable intelligent surface: Path loss modeling and experimental measurement," *IEEE Transactions on Wireless Communications*, vol. 20, no. 1, pp. 421–439, Jan. 2021.

[17] W. Tang, X. Chen, M. Chen, J. Dai, Y. Han, M. Di Renzo, S. Jin, Q. Cheng, T. Cui, "Path loss modeling and measurements for reconfigurable intelligent surfaces in the millimeter-wave frequency band," Jan. 2021. [Online]. Available: http://arxiv.org/abs/2101.08607.

[18] Ö. Özdogan, E. Björnson and E. G. Larsson, "Intelligent reflecting surfaces: Physics, propagation, and pathloss modeling," *IEEE Wireless Communications Letters*, vol. 9, no. 5, pp. 581–585, May 2020.

[19] Y. Sun, C. Wang, J. Huang and J. Wang, "A 3d non-stationary channel model for 6G wireless systems employing intelligent reflecting surfaces with practical phase shifts," *IEEE Transactions on Cognitive Communications and Networking*, vol. 7, no. 2, pp. 496–510, Jun. 2021.

[20] H. Jiang, C. Ruan, Z. Zhang, J. Dang, L. Wu, M. Mukherjee, D. B. da Costa, "A general wideband non-stationary stochastic channel model for intelligent reflecting surface-assisted MIMO communications," *IEEE Transactions on Wireless Communications*, vol. 20, no. 8, pp. 5314–5328, Aug. 2021.

[21] C. Cao, Z. Lian, Y. Wang, Y. Su and B. Jin, "A non-stationary geometry-based channel model for IRS-assisted UAV-MIMO channels," *IEEE Communications Letters*, vol. 25, no. 12, pp. 3760–3764, Dec. 2021.

[22] Z. Lian, Y. Su, Y. Wang and L. Jiang, "A non-stationary 3-d wideband channel model for intelligent reflecting surface-assisted HAP-MIMO communication systems," *IEEE Transactions on Vehicular Technology*, early access, doi: 10.1109/TVT.2021.3131765.

[23] H. Jiang, R. He, C. Ruan, J. Zhou and D. Chang, "Three-dimensional geometry-based stochastic channel modeling for intelligent reflecting surface-assisted UAV MIMO communications," *IEEE Wireless Communications Letters*, vol. 10, no. 12, pp. 2727–2731, Dec. 2021.

[24] E. Basar, "Reconfigurable intelligent surfaces for Doppler effect and multipath fading mitigation," Nov. 2020. [Online]. Available: https://arxiv.org/abs/1912.04080.

[25] B. Matthiesen, E. Björnson, E. De Carvalho and P. Popovski, "Intelligent reflecting surface operation under predictable receiver mobility: A continuous time propagation model," *IEEE Wireless Communications Letters*, vol. 10, no. 2, pp. 216–2220, Feb. 2021.

[26] B. Ai, R. He, H. Zhang, M. Yang, Z. Ma, G. Sun, and Z. Zhong, "Feeder communication for integrated networks," *IEEE Wireless Communications*, vol. 27, no. 6, pp. 20–27, Dec. 2020.

[27] Z. Lian, Y. Su, Y. Wang, L. Jiang, Z. Zhang, Z. Xie, and S. Li, "A non-stationary 3-d wideband channel model for low altitude UAV-MIMO communication systems," *IEEE Internet of Things Journal*, early access, doi: 10.1109/JIOT.2021.3108411.

[28] Z. Xiao, L. Zhu, Y. Liu, P. Yi, R. Zhang, X. Xia, and R. Schober, "A survey on millimeter-wave beamforming enabled UAV communications and networking," *IEEE Communications Surveys & Tutorials*, early access, doi: 10.1109/COMST.2021.3124512.

[29] Z. Xiao, L. Zhu and X. Xia, "UAV communications with millimeter-wave beamforming: Potentials, scenarios, and challenges," *China Communications*, vol. 17, no. 9, pp. 147–166, Sept. 2020.

[30] X. Cai, J. Rodríguez-Piñeiro, X. Yin, N. Wang, B. Ai, G. F. Pedersen, and A. P. Yuste, "An empirical air-to-ground channel model based on passive measurements in LTE," *IEEE Transactions on Vehicular Technology*, vol. 68, no. 2, pp. 1140–1154, Feb. 2019.

[31] X. Cai, T. Izydorczyk, J. Rodríguez-Piñeiro, I. Z. Kovács, J. Wigard, F. M. L. Tavares, and P. E. Mogensen, "Empirical low-altitude air-to-ground spatial channel characterization for cellular networks connectivity," *IEEE Journal on Selected Areas in Communications*, vol. 39, no. 10, pp. 2975–2991, Oct. 2021.

[32] X. Cai, C. Zhang, J. Rodríguez-Piñeiro, X. Yin, W. Fan and G. F. Pedersen, "Interference modeling for low-height air-to-ground channels in live LTE networks," *IEEE Antennas and Wireless Propagation Letters*, vol. 18, no. 10, pp. 2011–2015, Oct. 2019.

[33] S. Alfattani, W. Jaafar, Y. Hmamouche, H. Yanikomeroglu, A. Yongaçoglu, N. Đào, P. Zhu, "Aerial platforms with reconfigurable smart surfaces for 5G and beyond," *IEEE Communications Magazine*, vol. 59, no. 1, pp. 96–102, Jan. 2021.

[34] Q. Zhang, W. Saad and M. Bennis, "Reflections in the Sky: Millimeter wave communication with UAV-carried intelligent reflectors," in *Proc. IEEE GLOBECOM*, 2019, pp. 1–6.

[35] H. Lu, Y. Zeng, S. Jin and R. Zhang, "Aerial intelligent reflecting surface: Joint placement and passive beamforming design with 3d beam flattening," *IEEE Transactions on Wireless Communications*, vol. 20, no. 7, pp. 4128–4143, Jul. 2021.

[36] Z. Ma, B. Ai, R. He, C. Liu, N. Wang, M. Yang, Z. Zhong, W. Fan, "Multipath fading channel modeling with aerial intelligent reflecting surface," in *Proc. IEEE GLOBECOM*, 2021, pp. 1–6.

[37] Z. Ma, B. Ai, R. He, G. Wang, Y. Niu and Z. Zhong, "A wideband non-stationary air-to-air channel model for UAV communications," *IEEE*

Transactions on Vehicular Technology, vol. 69, no. 2, pp. 1214–1226, Feb. 2020.
[38] Z. Ma, B. Ai, R. He, G. Wang, Y. Niu, M. Yang, J. Wang, Y. Li, and Z. Zhong, "Impact of UAV rotation on MIMO channel characterization for air-to-ground communication systems," *IEEE Transactions on Vehicular Technology*, vol. 69, no. 11, pp. 12418–12431, Nov. 2020.
[39] Z. Ma, B. Ai, R. He, Z. Zhong and M. Yang, "A non-stationary geometry-based MIMO channel model for millimeter-wave UAV networks," *IEEE Journal on Selected Areas in Communications*, vol. 39, no. 10, pp. 2960–2974, Oct. 2021.
[40] A. F. Molisch, *Wireless Communications*, vol. 34. Hoboken, NJ, USA: Wiley, 2012.
[41] B. O. Hogstad, M. Pätzold, N. Youssef and D. Kim, "A MIMO mobile-to-mobile channel model: Part II–the simulation model," in *Proc. IEEE PIMRC*, 2005, pp. 1–6.
[42] F. Liu, O. Tsilipakos, A. Pitilakis, A. C. Tasolamprou, M. S. Mirmoosa, N. V. Kantartzis, D. H. Kwon, M. Kafesaki, C. M. Soukoulis, and S. A. Tretyakov, "Intelligent metasurfaces with continuously tunable local surface impedance for multiple reconfigurable functions," *Physical Review Applied*, vol. 11, no. 4, pp. 44024–44033, Apr. 2019.
[43] X. Chen, W. Xue, H. Shi, J. Yi and W. E. I. Sha, "Orbital angular momentum multiplexing in highly reverberant environments," *IEEE Microwave and Wireless Components Letters*, vol. 30, no. 1, pp. 112–115, Jan. 2020.
[44] X. Zhao, F. Du, S. Geng, Z. Fu, Z. Wang, Y. Zhang, Z. Zhou, L. Zhang, and L. Yang, "Playback of 5G and beyond measured MIMO channels by an ANN-based modeling and simulation framework," *IEEE Journal on Selected Areas in Communications*, vol. 38, no. 9, pp. 1945–1954, Sept. 2020.
[45] Z. Lian, L. Jiang, H. Chen, D. He, "A 3-d multiuser HAP-MIMO channel model based on dynamic evolution of LOS components," *Chinese Journal of Electronics*, vol. 28, no. 3, pp. 199–207, May 2019.
[46] L. Zhu, J. Zhang, Z. Xiao, X. Cao, D. Wu and X. Xia, "Millimeter-wave NOMA with user grouping, power allocation and hybrid beamforming," *IEEE Transactions on Wireless Communications*, vol. 18, no. 11, pp. 5065–5079, Nov. 2019.
[47] Z. Xiao, L. Zhu, J. Choi, P. Xia and X. Xia, "Joint power allocation and beamforming for non-orthogonal multiple access (NOMA) in 5G millimeter wave communications," *IEEE Transactions on Wireless Communications*, vol. 17, no. 5, pp. 2961–2974, May 2018.
[48] Z. Xiao, H. Dong, L. Bai, D. O. Wu and X. Xia, "Unmanned aerial vehicle base station (UAV-BS) deployment with millimeter-wave beamforming," *IEEE Internet of Things Journal*, vol. 7, no. 2, pp. 1336–1349, Feb. 2020.
[49] B. Fan, Y. Li, R. Zhang, Q. Fu, "Review on the technological development and application of UAV systems," *Chinese Journal of Electronics*, vol. 29, no. 2, pp. 199–207, Mar. 2020.

Zhangfeng Ma (Student Member, IEEE) received the B.Eng. degree in communication engineering from Huaihua University, Huaihua, Hunan, China, in 2015, the M.Sc. degree from the Chongqing University of Posts and Telecommunications (CQUPT), Chongqing, China, in 2018. He is currently working towards his Ph.D. degree in the School of Electronic and Information Engineering, Beijing Jiaotong University, Beijing, China. He is also a Visiting Ph.D. Student with the Antennas, Propagation and Millimetre-wave Systems (APMS) section, Department of Electronic Systems, Aalborg University, Aalborg, Denmark. His current research interests include wireless propagation channel modeling, non-stationary channel models, and unmanned aerial vehicle channel modeling. He received the IEEE VTC'19 Fall Best Student Paper Award in 2019.

Bo Ai (Fellow, IEEE) received the master's and Ph.D. degrees from Xidian University, China. He received the honor of Excellent Postdoctoral Research Fellow from Tsinghua University in 2007. He was a Visiting Professor with the Electrical Engineering Department, Stanford University, Stanford, CA, USA, in 2015. He is currently a Full Professor with Beijing Jiaotong University, where he is also the Deputy Director of the State Key Laboratory of Rail Traffic Control and Safety and the Deputy Director of the International Joint Research Center. He is one of the directors for Beijing "Urban Rail Operation Control System" International Science and Technology Cooperation Base, and the backbone member of the Innovative Engineering based jointly granted by the Chinese Ministry of Education and the State Administration of Foreign Experts Affairs.

He is the Research Team Leader of 26 national projects. He holds 26 invention patents. His interests include the research and applications of channel measurement and channel modeling and dedicated mobile communications for rail traffic systems. He has authored or co-authored eight books and authored over 300 academic research papers in his research area. Five papers have been the ESI highly cited paper. He has won some important scientific research prizes. He has been notified by the Council of Canadian Academies that based on the Scopus database, he has been listed as one of the Top 1% authors in his field all over the world. He has also been feature interviewed by the *IET Electronics Letters*.

Dr. Ai is a fellow of The Institution of Engineering and Technology and an IEEE VTS Distinguished Lecturer. He received the Distinguished Youth Foundation and Excellent Youth Foundation from the National Natural Science Foundation of China, the Qiushi Outstanding Youth Award by the Hong Kong Qiushi Foundation, the New Century Talents by the Chinese Ministry of Education, the Zhan Tianyou Railway Science and Technology Award by the Chinese Ministry of Railways, and the Science and Technology New Star by the Beijing Municipal Science and Technology Commission. He is an IEEE VTS Beijing Chapter Vice Chair and an IEEE BTS Xi' an Chapter Chair. He was a Co-Chair or a Session/Track Chair of many international conferences. He is an Associate Editor of the IEEE ANTENNAS AND WIRELESS PROPAGATION LETTERS, the IEEE TRANSACTIONS ON CONSUMER ELECTRONICS, and an Editorial Committee Member of the *Wireless Personal Communications Journal*. He is the Lead Guest Editor of special issues on the IEEE TRANSACTIONS ON VEHICULAR TECHNOLOGY, the IEEE ANTENNAS AND PROPAGATIONS LETTERS, and the *International Journal on Antennas and Propagations*.

Ruisi He (Senior Member, IEEE) received the B.E. and Ph.D. degrees from Beijing Jiaotong University (BJTU), Beijing, China, in 2009 and 2015, respectively.

Since 2015, Dr. He has been with the State Key Laboratory of Rail Traffic Control and Safety, BJTU, where he has been a Full Professor since 2018. Dr. He has been a Visiting Scholar in Georgia Institute of Technology, USA, University of Southern California, USA, and Université Catholique de Louvain, Belgium. His research interests include measurements and modeling of wireless channels, machine learning and clustering analysis in communications, vehicular and high-speed railway communications, 5G massive MIMO and high frequency communication techniques. He has authored/co-authored 4 books, 2 book chapters, more than 100 journal and conference papers, as well as several patents.

Dr. He is an Editor of the IEEE TRANSACTIONS ON WIRELESS COMMUNICATIONS, the IEEE ANTENNAS AND PROPAGATION MAGAZINE, the IEEE COMMUNICATIONS LETTERS, and a Lead Guest Editor of the IEEE JOURNAL ON SELECTED AREA IN COMMUNICATIONS, the IEEE TRANSACTIONS ON ANTENNAS PROPAGATION. He serves as the Early Career Representative (ECR) of Commission C, International Union of Radio Science (URSI). He has been a Technical Program Committee (TPC) chair and member for many conferences and workshops. He received URSI Issac Koga Gold Medal in 2020, the IEEE ComSoc Asia-Pacific Outstanding Young Researcher Award in 2019, the URSI Young Scientist Award in 2015, and five Best Paper Awards in conferences. He is a member of the COST.

Hang Mi (Student Member, IEEE) received the B.S. degree in Communication Engineering from North University of China in 2018. He is currently working towards the Ph.D. degree with the State Key Laboratory of Rail Traffic Control and Safety at Beijing Jiaotong University, China. His research interests are focused on radio propagation channel models, millimeter-wave channel modeling, and machine learning in wireless channels.

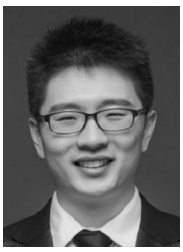

Mi Yang (Member, IEEE) received the M.S. and Ph.D. degrees from Beijing Jiaotong University, Beijing, China, in 2017 and 2021, respectively. He is currently an Associate Professor with the State Key Laboratory of Rail Traffic Control and Safety, Beijing Jiaotong University. His research interests include wireless propagation channels, vehicle-to-everything (V2X) communications, and 5G/B5G communications.

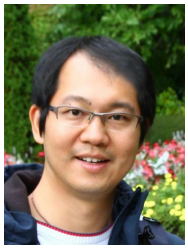

Ning Wang (Senior Member, IEEE) received the B.E. degree in communication engineering from Tianjin University, China, in 2004, the M.A.Sc. degree in electrical engineering from The University of British Columbia, Canada, in 2010, and the Ph.D. degree (Hons.) in electrical engineering from the University of Victoria, Victoria, Canada, in 2013. From 2004 to 2008, he was with the China Information Technology Design and Consulting Institute as a Mobile Communication System Engineer, specializing in planning and design of commercial mobile communication networks, network traffic analysis, and radio network optimization. He was a Post-Doctoral Research Fellow with the Department of Electrical and Computer Engineering, The University of British Columbia, from 2013 to 2015. Since 2015, he has been with the School of Information Engineering, Zhengzhou University, Zhengzhou, China, where he is currently an Associate Professor. He also holds adjunct appointments with the Department of Electrical and Computer Engineering, McMaster University, Hamilton, Canada, and the Department of Electrical and Computer Engineering, University of Victoria. His research interests include resource allocation and security designs of future cellular networks, channel modeling for wireless communications, statistical signal processing, and cooperative wireless communications. He was on the Finalist of the Governor General' s Gold Medal for Outstanding Graduating Doctoral Student with the University of Victoria in 2013. He has served on the technical program committees of international conferences, including the IEEE GLOBECOM, IEEE ICC, IEEE WCNC, and CyberC.

Zhangdui Zhong (Fellow, IEEE) received the B.E. and M.S. degrees from Beijing Jiaotong University, Beijing, China, in 1983 and 1988, respectively. He is a Professor and Advisor of Ph.D. candidates with Beijing Jiaotong University, Beijing, China. He is currently a Director of the School of Computer and Information Technology and a Chief Scientist of State Key Laboratory of Rail Traffic Control and Safety, Beijing Jiaotong University. He is also a Director of the Innovative Research Team of Ministry of Education, Beijing, and a Chief Scientist of Ministry of Railways, Beijing. He is an Executive Council Member of Radio Association of China, Beijing, and a Deputy Director of Radio Association, Beijing. His interests include wireless communications for railways, control theory and techniques for railways, and GSM-R systems. His research has been widely used in railway engineering, such as Qinghai-Xizang railway, Datong-Qinhuangdao Heavy Haul railway, and many high-speed railway lines in China.

He has authored or coauthored seven books, five invention patents, and over 200 scientific research papers in his research area. He received the MaoYiSheng Scientific Award of China, ZhanTianYou Railway Honorary Award of China, and Top 10 Science/Technology Achievements Award of Chinese Universities.

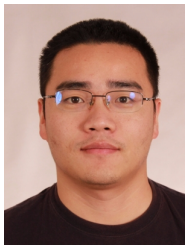

Wei Fan (Senior Member, IEEE) received the B.E. degree from the Harbin Institute of Technology, Harbin, China, in 2009, the double master's degree (Hons.) from the Politecnico di Torino, Turin, Italy, and the Grenoble Institute of Technology, Grenoble, France, in 2011, and the Ph.D. degree from Aalborg University, Aalborg, Denmark, in 2014. In 2011, he joined Intel Mobile Communications, Aalborg, Denmark, as a Research Intern. He conducted a three month internship with Keysight Technologies, Oulu, Finland, in 2014. He is currently an Associate Professor with Aalborg University, heading the research group Wireless propagation and Over the Air testing. His current research interests include over-the-air (OTA) testing of multiple antenna systems, radio channel sounding, parameter estimation, modeling and emulation and antenna measurement.